Gross-Pitaevskii Dynamics of Bose-Einstein Condensates and Superfluid Turbulence

M. E. Brachet [a] M. Abid [b] C. Huepe [c] S. Metens [d] C. Nore [e]
C. T. Pham [a] L. S. Tuckerman [e]

[a] *Laboratoire de Physique Statistique de l'Ecole Normale Supérieure, associé au CNRS et aux Universités Paris VI et VII, 24 Rue Lhomond, 75231 Paris, France*

[b] *Institut de Recherche sur les Phénomènes Hors Equilibre,U M R 6594 associé au CNRS et aux Universités d'Aix-Marseille I et II,49 rue Joliot Curie,13384 Marseille, France*

[c] *James Franck Institute, University of Chicago, 5640 S. Ellis Ave., Chicago IL 60637, USA*

[d] *Laboratoire de Physique Théorique de la Matière Condensée, Université Paris VII, 75005 Paris, France*

[e] *Laboratoire d'Informatique pour la Mécanique et les Sciences de l'Ingénieur, BP133, 91403 Orsay, France*

Abstract

The Gross-Pitaevskii equation, also called the nonlinear Schrödinger equation (NLSE), describes the dynamics of low-temperature superflows and Bose-Einstein Condensates (BEC). We review some of our recent NLSE-based numerical studies of superfluid turbulence and BEC stability. The relations with experiments are discussed.

Key words:

Contents

1	Introduction	2
2	Hydrodynamics using the NLSE	4
2.1	Madelung's transformation	4
2.2	Sound waves	6
2.3	Vortices in 2 and 3D	7

3 Superfluid turbulence 8

3.1 Tools for vortex dynamics 9

3.2 Numerical results 14

3.3 Experimental results 15

4 Stability of stationary solutions 18

4.1 Exact solution in 1D 18

4.2 General formulation 21

4.3 Branch following methods 23

4.4 Stability of a superflow around a cylinder 25

4.5 Stability of attractive Bose-Einstein condensates 35

5 Conclusion 41

6 Acknowledgments 41

References 41

1 Introduction

The present paper is a review of results, obtained by our group during the last 10 years, by numerically studying the nonlinear Schrödinger equation (NLSE). Direct numerical simulations (DNS) and branch-following methods were extensively used to investigate the dynamics and stability of NLSE solutions in 2 and 3 space dimensions.

Much work has been devoted to the determination of the critical velocity at which superfluidity breaks into a turbulent regime [1]. A mathematical model of superfluid ^{4}He, valid at temperatures low enough for the normal fluid to be negligible, is the nonlinear Schrödinger equation (NLSE), also called the Gross-Pitaevskii equation [2–4]. In a related context, dilute Bose-Einstein condensates (BEC) have been recently produced experimentally [5–7]. The dynamics of these compressible nonlinear quantum fluids is accurately described by the NLSE allowing direct quantitative comparison between theory and experiment [8].

Excitations of superfluid ^{4}He are described by the famous Landau spectrum which includes phonons in the low wave number range, and maxons and rotons

in the high (atomic-scale) wave number range. In contrast, the standard NLSE (the equation used in the present paper) used only phonon excitations. It therefore incompletely represents the atomic-scale excitations in superfluid ^4He. However, note that there exist generalizations of the NLSE [9,10] that do reproduce the correct excitation spectrum, at the cost of introducing a spatially non-local interaction potential.

Several problems pertaining to superfluidity and BEC can thus be studied in the framework of the NLSE. In this review, we concentrate on two such problems: (i) low-temperature superfluid turbulence [11–13] and (ii) stability of BEC in the presence of a moving obstacle [14–16] or an attractive interaction [17,18].

The authors recognize that this paper relates for the most part to their own work and does not include important and relevant contributions by other authors. However, we now give a short (and partial) list of references to provide a starting point to the reader motivated to undertake a deeper exploration of the field. A recent review of superfluid turbulence can be found in [19] and a proceeding devoted to the same subject is [20]. Alternate simulations (by Biot-Savart vortex methods) of low-temperature superfluid turbulence can be found in [21]. Reconnection and acoustic emission are studied in [22]. A standard reference on the subject of vortex reconnection is [23]. Cascade processes and Kelvin waves are investigated in [24–27] and [28]. Recent (very) low-temperature experiments in Helium are described in [29]. The experimental field of Bose-Einstein condensation is in rapid evolution. Recent results include the observation of an isolated quantum vortex [30,31] and the nucleation of several vortices [32]. Details of vortex dynamics [33] and even Kelvin waves [34] are now being observed.

The present paper is organized as follows: in section 2 the basic definitions and properties of the model of superflow are given. A short presentation of the hydrodynamic form, through Madelung's transformation, of NLSE with an arbitrary nonlinearity is derived. Simple solutions are discussed.

Section 3 is devoted to superfluid turbulence. The basic tools that are needed to numerically study 3D turbulence using NLSE are developed and validated in Section 3.1. The NLSE numerical results are given in section 3.2. Experimental results are given in section 3.3.

The stability of BEC is studied in section 4. Exact 1D results are given in section 4.1 and a general formulation of stability is given in section 4.2. Numerical branch-following methods are explained in section 4.3. The stability of a superflow around a cylinder is studied in section 4.4. The stability of an attractive Bose-Einstein condensate is studied in section 4.5. Finally, section 5 is our conclusion.

2 Hydrodynamics using the NLSE

The hydrodynamical form of NLSE with an arbitrary nonlinearity, corresponding to a barotropic fluid with an arbitrary equation of state, is introduced in this section. Basic hydrodynamical features such as acoustic propagation and stationary vortex solutions are also discussed.

2.1 Madelung's transformation

The connection between the NLSE and fluid dynamics can be obtained directly using the following action [35]:

$$\mathcal{A} = 2\alpha \int dt \left\{ \int d^3x \left(\frac{i}{2} \left(\overline{\psi} \frac{\partial \psi}{\partial t} - \psi \frac{\partial \overline{\psi}}{\partial t} \right) \right) - \mathcal{F} \right\} \tag{1}$$

with

$$\mathcal{F} = \int d^3x \left(\alpha |\nabla \psi|^2 + f(|\psi|^2) \right), \tag{2}$$

where $\psi(\vec{x}, t)$ is a complex wave field and $\overline{\psi}$ its complex conjugate, α is a positive real constant and f is a polynomial in $|\psi|^2 \equiv \overline{\psi}\psi$ with real coefficients:

$$f(|\psi|^2) = -\Omega|\psi|^2 + \frac{\beta}{2}|\psi|^4 + f_3|\psi|^6 + \ldots + f_n|\psi|^{2n}. \tag{3}$$

The NLSE is the Euler-Lagrange equation of motion for ψ corresponding to (1). It reads

$$\frac{\partial \psi}{\partial t} = -i \frac{\delta \mathcal{F}}{\delta \overline{\psi}},$$

or

$$\frac{\partial \psi}{\partial t} = i(\alpha \nabla^2 \psi - \psi f'(|\psi|^2)). \tag{4}$$

Madelung's transformation [1,35]

$$\psi = \sqrt{\rho} \exp\left(i \frac{\varphi}{2\alpha} \right) \tag{5}$$

maps the nonlinear wave dynamics of ψ into equations of motion for a fluid of density ρ and velocity $\vec{v} = \nabla\varphi$. Indeed, using equation (5), equation (1) can

be written as:

$$\mathcal{A} = -\int dt d^3x \left(\rho \frac{\partial \varphi}{\partial t} + \frac{1}{2}\rho(\nabla\varphi)^2 + 2\alpha f(\rho) + \frac{1}{2}(2\alpha\nabla(\sqrt{\rho}))^2 \right) \tag{6}$$

and the corresponding Euler-Lagrange equations of motion become:

$$\frac{\partial \rho}{\partial t} + \nabla \cdot (\rho \vec{v}) = 0, \tag{7}$$

$$\frac{\partial \varphi}{\partial t} + \frac{1}{2}(\nabla\varphi)^2 + 2\alpha f'(\rho) - 2\alpha^2 \frac{\Delta\sqrt{\rho}}{\sqrt{\rho}} = 0. \tag{8}$$

These equations are the continuity and Bernoulli equation [4] for an isentropic, compressible and irrotational fluid if one drops the last term of (8). This term is called the "quantum pressure".

Using this identification, one can define the following "thermodynamical functions" [1] . First, by inspecting the Bernoulli equation, the fluid's enthalpy per unit mass is given by:

$$h = 2\alpha f'(\rho). \tag{9}$$

Second, noting that $\frac{1}{2}\rho(\nabla\varphi)^2$ corresponds to kinetic energy in equation (6), the fluid's internal energy per unit mass reads:

$$e = \frac{2\alpha f(\rho)}{\rho}. \tag{10}$$

The general thermodynamic relation

$$h = e + p/\rho, \tag{11}$$

gives the expression

$$p = 2\alpha(\rho f'(\rho) - f(\rho)) \tag{12}$$

for the fluid's pressure.

The units of the variables used in (2) and (3) can be recovered as follows: Madelung's transformation (5) leads to $[|\psi|^2] = [\rho] = M\,L^{-3}$ and $[\alpha] = L^2\,T^{-1}$.Using (10), one gets $[f(\rho)/\rho] = T^{-1}$ and thus, from (3), $[\Omega] = T^{-1}$, $[\beta] = T^{-1}\,\rho^{-1}$ and $[f_i] = T^{-1}\,\rho^{1-i}$. Note that, in the case of a Bose condensate of particles of mass m, α has the value $\hbar/2m$ [36].

[1] Being isentropic ($S = 0$), the fluid is barotropic, and only one independent thermodynamic variable is needed.

2.2 Sound waves

2.2.1 Dispersion relation

The effect of the quantum pressure term in (8) can be found, at least to linear order, by means of the dispersion relation of acoustic (density) waves propagating in a constant density background ρ_0. Writing $\rho = \rho_0 + \delta\rho$ (with $f'(\rho_0) = 0$), $\nabla\varphi = \delta u$ in (7) and in the gradient of (8), one obtains (keeping only the linear terms):

$$\begin{aligned} \partial_t \delta\rho + \rho_0 \nabla \delta u &= 0 \\ \partial_t \delta u + 2\alpha f''(\rho_0)\nabla\delta\rho - 2\alpha^2 \Delta \frac{\nabla\delta\rho}{2\rho_0} &= 0 \end{aligned}$$

or

$$\partial_t{}^2 \delta\rho = 2\alpha\rho_0 f''(\rho_0)\Delta\delta\rho - \alpha^2\Delta^2\delta\rho.$$

The dispersion relation for an acoustic wave $\delta\rho = \epsilon(\exp(i(\omega t - \vec{k}\cdot\vec{x})) + c.c.)$ (with $\epsilon \ll 1$) is thus

$$\omega = \sqrt{2\alpha\rho_0 f''(\rho_0)\vec{k}^2 + \alpha^2\vec{k}^4}. \tag{13}$$

It is clear from this relation that the quantum pressure has a noticeable dispersive effect for large wave numbers. For small wave numbers, the usual propagation, with a constant speed of sound given by:

$$c = \left(\frac{\partial p}{\partial \rho}\right)^{\frac{1}{2}} = \sqrt{2\alpha\rho_0 f''(\rho_0)},$$

is recovered. The length scale $\xi = \sqrt{\alpha/(\rho_0 f''(\rho_0))}$ at which dispersion becomes noticeable is known as the coherence length.

2.2.2 Nonlinear acoustics

The description given by linear acoustics can be somewhat improved by including the dominant nonlinear effects. Such an equation was derived in [37].

Numerical simulations of NLSE in one space dimension using a standard Fourier pseudo-spectral method [38] can be used to study the acoustic regime

triggered by an initial disturbance of the form :

$$\psi(x) = 1 + ae^{-\frac{x^2}{l^2}}.$$

Such simulations were performed in ref. [37] where it was found that the shocks which would have appeared under compressible Euler dynamics (i.e. following equation (8) without the last term in l.h.s.) are regularized by the dispersion. There was no evidence of finite-time singularity in our numerics: the spectrum of the solution was well resolved, with a conspicuous exponential tail.

2.3 Vortices in 2 and 3D

Stationary solutions of the equations of motion can give more insight into the connection between the NLSE and fluid dynamics. Indeed, stationary solutions of NLSE (4) are also solutions of the Real Ginzburg-Landau Equation (RGLE)

$$\frac{\partial \psi}{\partial t} = -\frac{\delta \mathcal{F}}{\delta \overline{\psi}} = (\alpha \nabla^2 \psi - \psi f'(|\psi|^2)). \tag{14}$$

They are thus extrema of the free energy $\mathcal{F}$.

The simplest solution of this type corresponds to a constant density fluid at rest. Therefore, ψ is constant in space and (14) reads:

$$f'(|\psi|^2) = -\Omega + \beta|\psi|^2 + 3f_3|\psi|^4 + \ldots + nf_n|\psi|^{2n-2} = 0. \tag{15}$$

This equation, for given values of the coefficients β and $f_i, i = 3, \ldots, n$, fixes the Ω term of f by the fluid's density $|\psi|^2$. However, Ω could be removed from the Bernoulli equation (8) by the change of variable $\varphi \to \varphi + 2\alpha\Omega t$ that corresponds to a change of phase $\psi \to \psi e^{i\Omega t}$ in NLSE (4). Thus, Ω does not play an important role in the NLSE dynamics. It is however a matter of convention not to perform these changes of variable in order that stationary solutions of (14) coincide with those of (4).

Vortex solutions are another important kind of stationary solutions of NLSE. They are topological defects, or singularities, of Madelung's transformation when $\rho = 0$ (i.e. when both $\Re(\psi) = 0$ and $\Im(\psi) = 0$). These two conditions localize singularities into points in two dimensions and lines in three dimensions. The circulation of $\vec{v}$ around such a generic singularity is $\pm 4\pi\alpha$. Therefore, they are known in the framework of superfluidity as *quantum vortices* [1]. Solutions of (14) with cylindrical symmetry are obtained numerically in [39]. It is found that the density profile of a vortex admits a horizontal

tangent near the core while the velocity diverges as the inverse of the core distance. The momentum density $\rho\vec{v}$ is thus a regular quantity. It is important to realize that such vortex solutions are *regular* solutions of the NLSE (4), the singularity stemming only from Madelung's transformation (5).

3 Superfluid turbulence

The mathematical description of superfluid flows (*i.e.* laboratory ^{4}He flows) is based on Landau's two-fluid model [4]. The interaction of normal fluid and superfluid vortices is called *mutual friction* and must be taken into account as pioneered by Schwarz [40]. At sufficiently low temperatures, one can neglect the normal fluid (below $T = 1^\circ K$ for helium at normal pressure) and another mathematical description is given by the Nonlinear Schrődinger Equation NLSE (or Gross-Pitaevskii equation [2,3]). Note that it is difficult to estimate the precise temperature below which the normal component can be neglected. There remains an urgent need for more experiments at much lower temperatures such as those reported in [29].

In this section, we will use the simplest form for f, corresponding to a cubic nonlinearity in the NLSE (4). The NLSE, with convenient normalization, then reads:

$$\partial_t\psi = (ic/\sqrt{2}\xi)(\psi - |\psi|^2\psi + \xi^2\nabla^2\psi). \tag{16}$$

Madelung's transformation (5) takes the form

$$\rho = |\psi|^2 \tag{17}$$

$$\rho v_j = (ic\xi/\sqrt{2})(\psi\partial_j\overline{\psi} - \overline{\psi}\partial_j\psi) \tag{18}$$

where ξ and c are the coherence length defined above and speed of sound (when $\rho_0 = 1$ [1]) respectively. The superflow is irrotational everywhere but near the lines $\psi = 0$ (topological defects). There, the flow evolves under Eulerian dynamics [41,42]. The topological defect lines are the superfluid vortices, whose velocity circulation is automatically correct in this model [36].

The present section is devoted to the analogy between turbulence in low–temperature superfluids and classical turbulence in incompressible viscous fluids. This is done numerically by conducting numerical simulations of NLSE for the Taylor-Green (TG) vortex [43] and comparing the results with prior Navier-Stokes simulations for the same vortex. The well-documented TG vortex [44–46] is the solution of the Navier-Stokes equations with initial velocity field:

$$\mathbf{v}^{TG} = \Big(\sin(x)\cos(y)\cos(z), -\cos(x)\sin(y)\cos(z), 0 \Big). \tag{19}$$

It admits symmetries that are used to speed up computations: rotation by π about the axis $(x = z = \pi/2)$, $(y = z = \pi/2)$ and $(x = y = \pi/2)$ and reflection symmetry with respect to the planes $x = 0, \pi$, $y = 0, \pi$, $z = 0, \pi$. The velocity is parallel to these planes which form the sides of the *impermeable box* which confines the flow.

3.1 Tools for vortex dynamics

It is well known that compressible fluid dynamics, with an arbitrary chosen initial condition, leads to a flow dominated by acoustic radiation. We must thus generate an initial data with as small acoustic emission as possible if we are to use NLSE to study vortex dynamics.

3.1.1 Preparation method

We now present a method for generating a vortex array whose NLSE dynamics is similar to the classical vortex dynamics of the large scale flow $\mathbf{v}^{TG}$. Our method has two steps. In the first, we exhibit a global Clebsch representation of $\mathbf{v}^{TG}$. The acoustic wave emission is minimized in the second step [47].

The Clebsch potentials:

$$\lambda(x, y, z) = \cos(x)\sqrt{2 \mid \cos(z) \mid} \tag{20}$$

$$\mu(x, y, z) = \cos(y)\sqrt{2 \mid \cos(z) \mid}\, \mathrm{sgn}(\cos(z)) \tag{21}$$

(where sgn gives the sign of its argument) correspond to the TG flow in the sense that $\nabla \times \mathbf{v}^{TG} = \nabla\lambda \times \nabla\mu$ and λ and μ are periodic functions of (x, y, z). These Clebsch potentials map the physical space (x, y, z) into the (λ, μ) plane. The complex field ψ_c , corresponding to the large scale TG flow circulation, is given by $\psi_c(x, y, z) = (\psi_4(\lambda, \mu))^{[\gamma_d/4]}$ with $\gamma_d = 2\sqrt{2}/(\pi c\xi)$ ([ ] denotes the integer part of a real) and

$$\begin{aligned} \psi_4(\lambda, \mu) = \psi_e(\lambda - 1/\sqrt{2}, \mu)\psi_e(\lambda, \mu - 1/\sqrt{2}) \times \\ \psi_e(\lambda + 1/\sqrt{2}, \mu)\psi_e(\lambda, \mu + 1/\sqrt{2}) \end{aligned} \tag{22}$$

where $\psi_e(\lambda, \mu) = (\lambda + i\mu)\tanh(\sqrt{\lambda^2 + \mu^2}/\sqrt{2}\xi)/\sqrt{\lambda^2 + \mu^2}$.

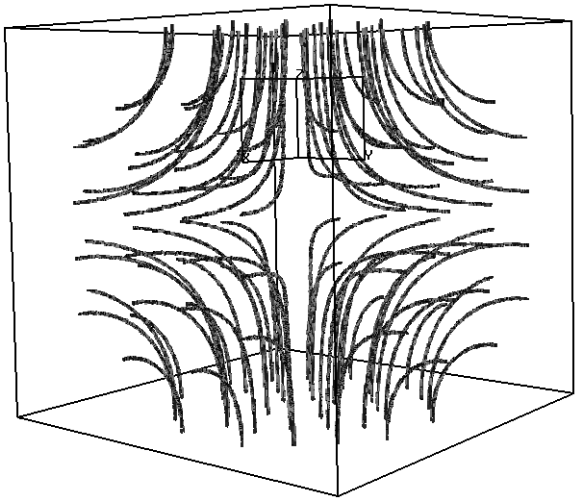

Fig. 1. Three-dimensional visualization of the vector field $\nabla \times (\rho \vec{v})$ for the Taylor-Green flow at time $t = 0$ with coherence length $\xi = 0.1/(8\sqrt{2})$, sound velocity $c = 2$ and $N = 512$ in the impermeable box $[0, \pi] \times [0, \pi] \times [0, \pi]$.

The second step of our procedure consists of integrating, to convergence, the Advective Real Ginzburg-Landau Equation (ARGLE):

$$\partial_t \psi = c/(\sqrt{2}\xi)(\psi - |\psi|^2\psi + \xi^2\nabla^2\psi) - i\mathbf{v}^{TG} \cdot \nabla\psi - (\mathbf{v}^{TG})^2/(2\sqrt{2}c\xi)\psi \tag{23}$$

with initial data $\psi = \psi_c$.

Using the TG symmetries we expand $\psi(x, y, z, t)$, solution of the ARGLE and NLSE equations, as [11]:

$$\psi(x, y, z, t) = \sum_{m=0}^{N/2} \sum_{n=0}^{N/2} \sum_{p=0}^{N/2} \hat{\psi}(m, n, p, t) \cos mx \cos ny \cos pz \tag{24}$$

where N is the resolution and $\hat{\psi}(m, n, p, t) = 0$, unless m, n, p are either all even or all odd integers. Furthermore $\hat{\psi}(m, n, p, t)$ satisfies the additional conditions $\hat{\psi}(m, n, p, t) = (-1)^{r+1}\hat{\psi}(n, m, p, t)$ where $r = 1$ when m, n, p are all even and $r = 2$ when m, n, p are all odd. Implementing this expansion in a pseudo–spectral code yields a saving of a factor 64 in computational time and memory size when compared to general Fourier expansions.

The ARGLE converged periodic vortex array obtained in this manner is displayed on Fig. 1. with coherence length $\xi = 0.1/(8\sqrt{2})$, sound velocity $c = 2$ and resolution $N = 512$.

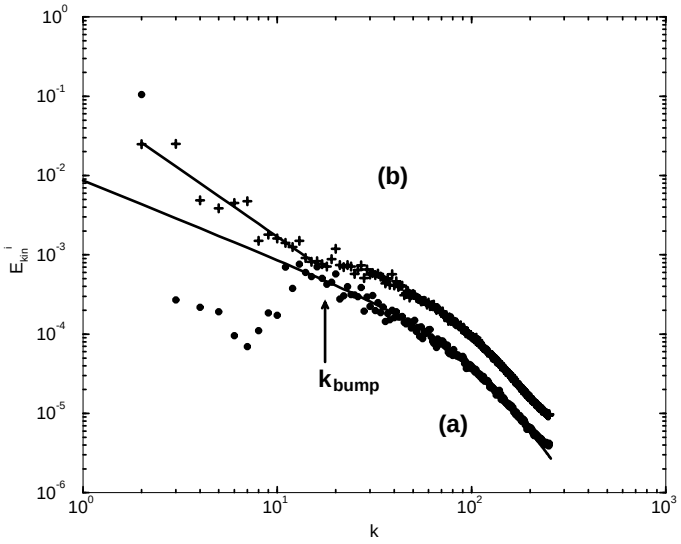

Fig. 2. Plot of the incompressible kinetic energy spectrum, $E^i_{kin}(k)$. The bottom curve (a) (circles) corresponds to time $t = 0$. The spectrum of a single axisymmetric 2D vortex multiplied by $(l/2\pi) = 175$ is shown as the bottom solid line. The top curve (b) (pluses) corresponds to time $t = 5.5$. A least-square fit over the interval $2 \leq k \leq 16$ with a power law $E^i_{kin}(k) = Ak^{-\,n}$ gives $n = 1.70$ (top solid line).

3.1.2 Energy spectra

The total energy of the vortex array, conserved by NLSE dynamics, can be decomposed into three parts $E_{tot} = (1/2\pi)^3 \int d^3x(\mathcal{E}_{kin} + \mathcal{E}_{int} + \mathcal{E}_q)$, with kinetic energy $\mathcal{E}_{kin} = \rho v_j v_j/2$, internal energy $\mathcal{E}_{int} = (c^2/2)(\rho - 1)^2$ and quantum energy $\mathcal{E}_q = c^2\xi^2(\partial_j\sqrt{\rho})^2$. Each of these parts can be defined as the integral of the square of a field, for example, $\mathcal{E}_{kin} = (\sqrt{\rho}v_j)^2/2$. In order to separate the kinetic energy corresponding to compressibility effects, $\mathcal{E}_{kin}$ can be further decomposed into a compressible and incompressible parts using $\sqrt{\rho}v_j = (\sqrt{\rho}v_j)^c + (\sqrt{\rho}v_j)^i$ with $\nabla.(\sqrt{\rho}v_j)^i = 0$. Using Parseval's theorem, the angle-averaged kinetic energy spectrum is written as:

$$E_{kin}(k) = \frac{1}{2}\int k^2 \sin\theta d\theta d\phi \left| \frac{1}{(2\pi)^3}\int d^3r e^{ir_j k_j}\sqrt{\rho}v_j \right|^2$$

which verifies $E_{kin} = (1/2\pi)^3 \int d^3x\mathcal{E}_{kin} = \int_0^\infty dk E_{kin}(k)$. The angle-averaged spectrum is obtained by summation over shells in Fourier space. A mode (m, n, p) belongs to the shell numbered $k = [\sqrt{m^2 + n^2 + p^2} + 1/2]$.

Note that the radius of curvature of the vortex lines in Fig. 1 is large compared to their radii. Thus these 3D lines can be considered as straight, and then compared to the 2D axisymmetric vortices which are exact solutions to the 2D NLSE. A 2D vortex at the origin can be written as $\psi^{vort}(r) = \sqrt{\rho(r)}\exp(im\varphi)$,

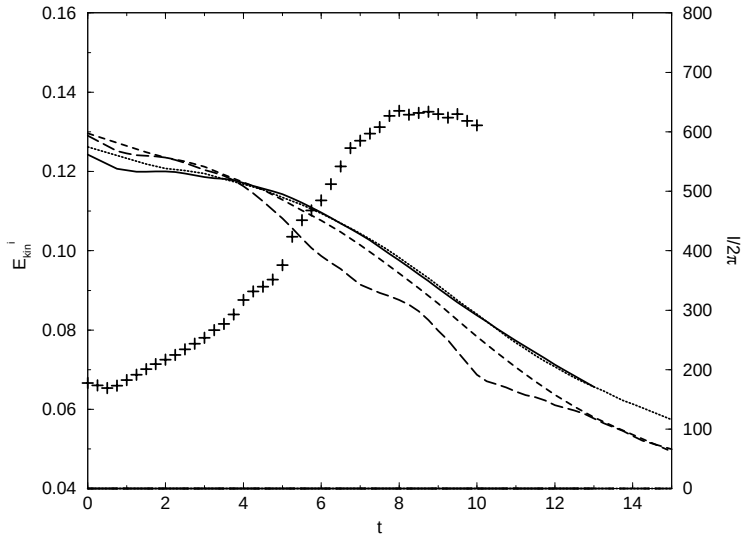

Fig. 3. Total incompressible kinetic energy, E^i_{kin}, plotted versus time for $\xi = 0.1/(2\sqrt{2})$, $N = 128$ (long–dash line); $\xi = 0.1/(4\sqrt{2})$, $N = 256$ (dash); $\xi = 0.1/(6.25\sqrt{2})$, $N = 400$ (dot) and $\xi = 0.1/(8\sqrt{2})$, $N = 512$ (solid line). All runs are realized with $c = 2$. The evolution of the total vortex filament length divided by 2π (crosses) for the $N = 512$ run is also shown (scale given on the right y-axis).

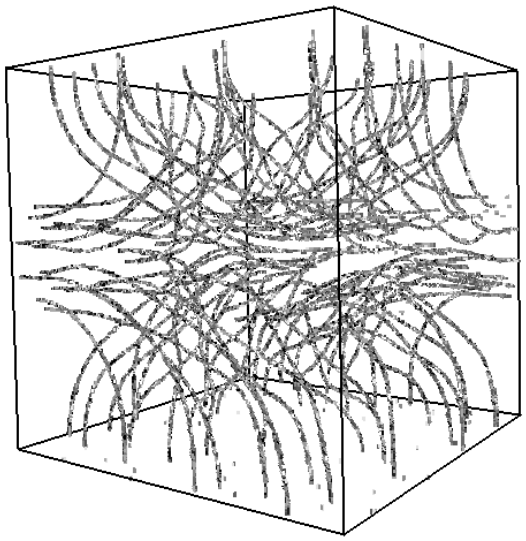

Fig. 4. Same visualization as in Fig. 1 but at time $t = 4$.

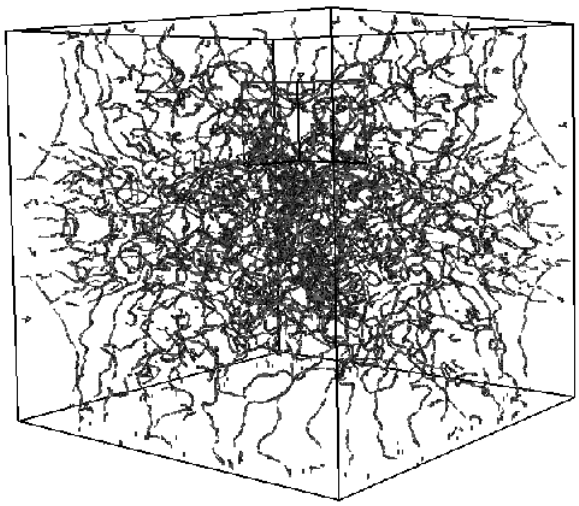

Fig. 5. Same visualization as in Fig. 1 but at time $t = 8$.

$m = \pm 1$, where (r, φ) are polar coordinates. The vortex profile admits different limits $\sqrt{\rho(r)} \sim r$ as $r \to 0$ and $\sqrt{\rho(r)} = 1 + O(r^{-2})$ for $r \to \infty$. It can be computed numerically using mapped Chebychev polynomials and an appropriate functional [11]. The corresponding velocity field is azimuthal and is given by $v(r) = \sqrt{2}c\xi/r$. Using the mapped Chebychev polynomials expansion for $\sqrt{\rho(r)}$, the angle averaged spectrum of $\sqrt{\rho}v_j$ can then be computed with the formula $E_{kin}^{vort}(k) = (c^2\xi^2/2\pi k)\left(\int_0^\infty dr J_0(kr)\partial_r\sqrt{\rho}\right)^2$ [11], where J_0 is the zeroth order Bessel function.

The incompressible kinetic energy spectrum E_{kin}^{i} of the ARGLE converged vortex array of Fig. 1 is displayed on Fig. 2. For large wavenumbers, the spectrum is well represented by extending a collection of 2D vortices into 3D vortex lines via $E_{kin}^{line}(k) \equiv const. \times E_{kin}^{vort}(k)$. (We will see that the constant of proportionality is related to the length l of vortex lines by $const. = l/(2\pi) = 175$ at time $t = 0$.) In contrast, the small wavenumber region cannot be represented by E_{kin}^{line}. This stems from the average separation distance between the vortex lines in Fig. 1. Denoting this distance $d_{bump} = k_{bump}^{-1} = 1/16$, the wavenumber range between the large-scale wavenumber $k = 2$ and the characteristic separation wavenumber k_{bump} can be explained by interference effects. Due to constructive interference, the energy spectrum at $k = 2$ has a value close to its corresponding value in TG viscous flow (namely 0.125), which greatly exceeds the value of $E_{kin}^{line}(k = 2)$. In contrast, for $2 < k \leq k_{bump}$, destructive interference decreases E_{kin}^{i} below E_{kin}^{line}.

3.2 Numerical results

The evolution in time via NLSE (16) of the incompressible kinetic energy is shown in Fig. 3. The main quantitative result is the excellent agreement of the energy dissipation rate, $-dE^i_{kin}/dt$, with the corresponding data in the incompressible viscous TG flow (see reference [44], and reference [48], figure 5.12). Both the moment $t_{max} \sim 5 - 10$ of maximum energy dissipation (the inflection point of Fig. 3) and its value $\epsilon(t_{max}) \sim 10^{-2}$ at that moment are in quantitative agreement. Furthermore, both t_{max} and $\epsilon(t_{max})$ depend weakly on ξ.

Another important quantity studied in viscous decaying turbulence is the scaling of the kinetic energy spectrum during time evolution and, especially, at the moment of maximum energy dissipation, where a $k^{-5/3}$ range can be observed (see reference [44]). Fig. 2 (b) shows the energy spectrum at $t = 5.5$. A least-square fit over the interval $2 \leq k \leq 16$ with a power law $E^i_{kin}(k) = Ak^{-\ n}$ gives $n = 1.70$ (solid line). For $5 < t < 8$, a similar fit gives $n = 1.6 \pm 0.2$ (data not shown). Note that recent numerical simulations [49] using incompressible Eulerian dynamics of vortex filaments also show evidence of a $k^{-5/3}$ energy spectrum range.

The full Kolmogorov law is given by $E(k) = C\varepsilon^{2/3}k^{-5/3}$ with $E(k)$ the energy spectrum (per unit mass), C the Kolmogorov constant and ε the energy dissipation rate (per unit mass). The viscous energy spectrum $E(k)$ is comparable (see ref. [44]), in the inertial range, to the superfluid incompressible kinetic energy $E^i_{kin}(k)$. As stated above, the superfluid dissipation rate $-dE^i_{kin}/dt$ is also comparable to the viscous dissipation rate ε. Therefore, the Kolmogorov constant C is of the same order of magnitude in both viscous and superfluid flows. Note that the viscous Taylor-Green vortex, because of the non-homogenous character of the flow, has a Kolmogorov constant that is larger (by a factor $\simeq 1.5$) [44] than that of homogeneous turbulence.

Fitting $E^i_{kin}(k)$ in the interval $30 \leq k \leq 170$ with $l/(2\pi) \times E^{vort}_{kin}(k)$ leads to $l/2\pi = 452$, roughly three times the $t = 0$ length of the vortex lines. The time evolution of $l/2\pi$ obtained by this procedure is displayed in Fig. 3, showing that the length continues to increase beyond t_{max}. The computations were performed with $c = 2$ corresponding to a *root-mean-square* Mach number $M_{rms} \equiv |\mathbf{v}^{TG}_{rms}|/c = 0.25$. As it is very costly to decrease M_{rms}, we checked [11] that compressible effects were non-dominant at this value of M_{rms}.

The vortex lines are visualized in physical space in Figs. 4 and 5 at time $t = 4$ and $t = 8$. At $t = 4$, no reconnection has yet taken place while a complex vortex tangle is present at $t = 8$. Detailed visualizations (data not shown) demonstrate that reconnections occur for $t > 5$. Note that the viscous

TG vortex also undergoes a qualitative (and quantitative) change in vortex dynamics around $t \sim 5$.

3.3 Experimental results

The TG flow is related to an experimentally studied swirling flow [50–52]. The relation between the experimental flow and the TG vortex is a similarity in overall geometry [50]: a shear layer between two counter–rotating eddies. The TG vortex, however, is periodic with free-slip boundaries while the experimental flow is contained inside a tank between two counter–rotating disks.

The spectral behavior of NLSE can be compared to standard (viscous) turbulence only for $k \leq k_{bump}$. It is thus of interest to estimate the scaling of k_{bump} in terms of the characteristic parameters of the large scale flow and of the fluid. As seen above, $k_{bump} \sim d_{bump}^{-1}$, where d_{bump} is the average distance between neighboring vortices. Consider a flow with characteristic integral scale l_0 and large scale velocity u_0 (in the case of the TG flow, $l_0 \sim 1$ and $u_0 \sim 1$). The fluid characteristics are the velocity of sound c and the coherence length ξ (with corresponding wavenumber $k_\xi \sim \xi^{-1}$). The number n_d of vortex lines crossing a typical large–scale l_0^2 area is given by the ratio of the large–scale flow circulation $l_0 u_0$ to the quantum of circulation $\Gamma = 4\pi c\xi/\sqrt{2}$, i.e $n_d \sim l_0 u_0/c\xi$. On the other hand, the assumption that the vortices are uniformly spread over the large scale area gives $n_d \sim l_0^2/d_{bump}^2$. Equating these two evaluations of n_d yields the relation $d_{bump} \sim l_0\sqrt{(c\xi)/(l_0 u_0)}$. Note that this argument assumes that the large-scale vorticity is coherent. It therefore yields a maximum possible value of d_{bump}, and thus a minimum for k_{bump}.

In the case of helium, the viscosity at the critical point ($T = 5.174°K$, $P = 2.2\ 10^5\ Pa$) is $\nu_{cp} = 0.27 \times 10^{-7} m^2 s^{-1}$ while the quantum of circulation, $\Gamma = h/m_{He}$ has the value $0.99 \times 10^{-7} m^2 s^{-1}$. Thus, $\nu_{cp} \sim 0.25\Gamma$. The order of magnitude for d_{bump} is thus $d_{bump} \simeq l_0/\sqrt{R_{cp}} \sim l_\lambda$ where R_{cp} is the integral scale Reynolds number at the critical point and l_λ the Taylor micro-scale. In other words, the value of d_{bump} in a superfluid helium experiment at $T = 1°K$ is of the same order as the Taylor micro-scale in the same experimental set-up run with viscous helium at the critical point.

The experimental set-up is similar to that described in [51]. To work with $T \sim 1.2K$ some modifications are, however, necessary. A cylinder, 8 cm in diameter and 12 cm high, limited axially by two counter-rotating disks limits the flow. One disk is flat and 8 radial blades, forming an angle of 45^o between each other, are fixed on the other one. To stabilize the turbulent shear region a stator is mounted halfway the height of the container. The two disks are driven by two DC motors rotating from 1 to 30 Hz. The whole system is enclosed

in a liquid Helium bath used as the experimental fluid and this is the main difference with the set-up described in [51]. The pressure above the liquid bath is adjusted by a pumping system and this fixes the temperature of the fluid.

Local pressure fluctuations are measured by using small total-head pressure tubes, immersed in the flow. The pressure sensors are hollow metallic tubes, connected to a quartz pressure transducer WHM 112 A22 from PCB. Details are given in [13].

In normal fluids, the pressure measured at the tip of the total-head tube can be related to the upstream flow $U(t)$ and the local pressure $P(t)$ using Bernoulli theorem:

$$P_{\rm meas}(t) = P(t) + \rho U^2(t)/2 \tag{25}$$

In the flow region where the probe is immersed, a well established axial mean flow U exists so that, after removing the mean parts of equation (25), one gets:

$$p_{\rm meas}(t) = p(t) + \rho U u(t) \tag{26}$$

where $p_{\rm meas}$, p and u are the fluctuations of the measured pressure, the actual pressure, and the local velocity respectively. It is currently admitted that, in ordinary turbulent situations, and at low fluctuation rates, equation (26) is dominated by the dynamic term, so that, by measuring the pressure fluctuations at the total head tube, one has a direct access to the velocity fluctuations $u(t)$.

The situation is less clear when the probe is immersed in the superfluid. It is, however, possible to write an equation similar to (26). Details can be found in [13].

The analysis of the pressure fluctuations obtained with the total head tube placed at 2 cm above the mid plane and 2 cm from the cylinder axis, yields interesting conclusions. Figures 6 and 7 show the spectra of the pressure fluctuations above and below T_λ (i.e respectively at $2.3K$ and $1.4K$). Fig. 6 clearly shows, as expected, that such fluctuations follow a Kolmogorov regime between the injection scale (signaled by the peak at 25 Hz) and the largest resolved frequency, i.e 900 Hz. The spectrum obtained at $1.4K$ is similar to that obtained at $T = 2.3K$ (see Fig. 7). A clear Kolmogorov like regime exists for the same range of frequencies. The corresponding Kolmogorov constant turns out also to be indistinguishable from the classical value. We have further analyzed the deviations from Kolmogorov in the superfluid regime. The striking result is that they have the same magnitude as in classical turbulence. More details are given in [53].

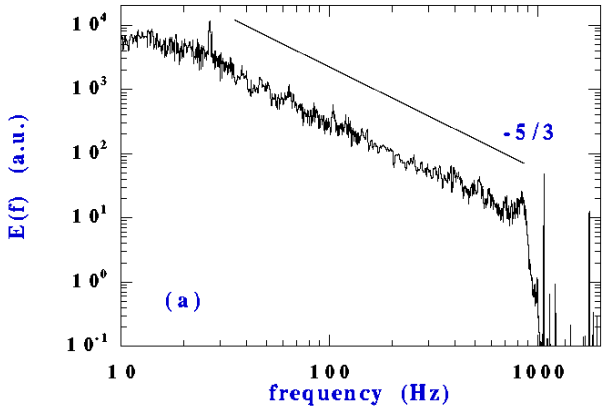

Fig. 6. Experimental pressure fluctuation spectrum (in non-dimensional units) measured with a total head pressure tube immersed in the flow at $T = 2.3\ K$.

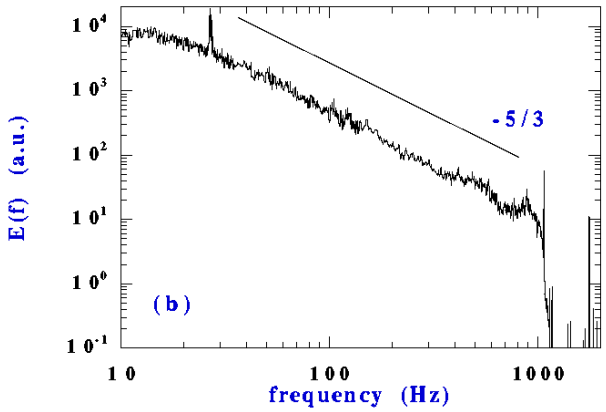

Fig. 7. Experimental pressure fluctuation spectrum (in non-dimensional units) measured with a total head pressure tube immersed in the flow at $T = 1.4\ K$.

These observations - both on global and local quantities - agree well with the theoretical approach developed in the previous section. In particular, it seems clear that the Kolmogorov cascade survives in the superfluid regime.

4 Stability of stationary solutions

This section is devoted to the stability of BEC. Exact 1D bifurcation results are given in section 4.1. A general formulation of stability is presented in section 4.2. Numerical branch following methods are explained in section 4.3. The stability of a superflow around a cylinder is investigated in section 4.4 and attractive Bose-Einstein condensates are studied in section 4.5.

4.1 Exact solution in 1D

4.1.1 Definition of the system

We consider a point impurity moving within a 1D superflow. In the frame of the moving impurity, the system can be described by the following action functional

$$\mathcal{A}[\psi,\overline{\psi}] = \int \mathrm{d}t \left[\frac{i}{2} \int \mathrm{d}x \, (\overline{\psi}\partial_t\psi - \psi\partial_t\overline{\psi}) - \mathcal{K} \right] . \tag{27}$$

In this expression, ψ is a complex field, $\overline{\psi}$ its conjugate and the energy functional $\mathcal{K}$ reads

$$\mathcal{K} = \mathcal{E} - v\mathcal{P} + v\left[R^2(+\infty)\phi(+\infty) - R^2(-\infty)\phi(-\infty)\right] , \tag{28}$$

with

$$\mathcal{E} = \int \mathrm{d}x \, \left[|\partial_x\psi|^2 + \frac{1}{2}(|\psi|^2-1)^2 + g\delta(x)(|\psi|^2-1) \right] , \tag{29}$$

$$\mathcal{P} = \int \mathrm{d}x \, \frac{1}{2i} \left[\overline{\psi}(\partial_x\psi) - \psi(\partial_x\overline{\psi}) \right] , \tag{30}$$

$$\psi = R\exp(i\phi) . \tag{31}$$

The Dirac (pseudo) potential $g\delta(x)$ in (29) represents the impurity and the last term in (28) imposes the appropriate boundary conditions for the phase ϕ [54]. R obeys the boundary conditions $R^2(\pm\infty) = 1$.

The Euler-Lagrange equation associated to (27), $\delta\mathcal{A}/\delta\overline{\psi} = 0$, is the nonlinear Schrödinger equation (NLSE)

$$i\partial_t\psi = -\partial_{xx}\psi + iv\,\partial_x\psi - \psi + |\psi|^2\psi + g\delta(x)\psi , \tag{32}$$

where the jump condition

$$\partial_x\psi(0^+,t) - \partial_x\psi(0^-,t) = g\psi(0,t) \tag{33}$$

is imposed in order to balance the $g\delta(x)\psi$ singularity with the $-\partial_{xx}\psi$ term for all times t.

4.1.2 Stationary solutions

Time-independent solutions of the NLSE (32) are best studied by performing the change of variables defined above in (31): $\psi = R\exp(i\phi)$. Using these variables, the NLSE reads

$$\partial_t R = v\partial_x R - R\partial_{xx}\phi - 2\partial_x R\partial_x\phi\,, \tag{34}$$

$$\partial_t\phi = v\partial_x\phi - (\partial_x\phi)^2 + 1 - R^2 - g\delta(x) + \frac{\partial_{xx}R}{R}\,, \tag{35}$$

and the jump condition (33) reads

$$\partial_x R(0^+,t) - \partial_x R(0^-,t) = gR(0,t)\,, \tag{36}$$

$$\partial_x\phi(0^+,t) - \partial_x\phi(0^-,t) = 0\,. \tag{37}$$

Note that equations (34) and (35) can be respectively interpreted as the continuity and Bernoulli equations for a fluid of density $\rho = R^2(x)$ and velocity $u = 2\partial_x\phi$ (as done in section 2).

Explicit time-independent solutions of equations (34) and (35) were found by Hakim[54], using what are called *gray solitons* in the nonlinear optics terminology. Gray solitons [55,56] are stationary solutions of equations (34) and (35), *without* the potential term $g\delta(x)$. They are localized density depletion of the form

$$R^2_{\rm GS}(x) = v^2/2 + (1 - v^2/2)\tanh^2[\sqrt{1/2 - v^2/4}\,x]\,, \tag{38}$$

$$\phi_{\rm GS}(x) = \arctan\left(\frac{v\sqrt{2-v^2}}{\exp[\sqrt{2-v^2}\,x] + v^2 - 1}\right). \tag{39}$$

Patching together pieces of gray solitons, Hakim found the following ξ-indexed stationary solutions of equations (34) and (35), *including* the potential term $g\delta(x)$

$$R_\xi(x) = R_{\rm GS}(x \pm \xi)\,, \qquad x \gtrless 0 \tag{40}$$

$$\phi_\xi(x) = \phi_{\rm GS}(x \pm \xi) - \phi_{\rm GS}(\pm\xi)\,, \qquad x \gtrless 0 \tag{41}$$

where the jump conditions (36) and (37) impose the relation

$$g(\xi) = \sqrt{2}(1 - v^2/2)^{3/2}\frac{\tanh[\sqrt{1/2 - v^2/4}\,\xi]}{v^2/2 + \sinh^2[\sqrt{1/2 - v^2/4}\,\xi]}\,. \tag{42}$$

The function $g(\xi)$ reaches a maximum [57] $g_c = g(\xi_c)$ at $\xi_c = \frac{\operatorname{argcosh}\left(\frac{1+\sqrt{1+4v^2}}{2}\right)}{\sqrt{2-v^2}}$ with

$$g_c = 4(1 - v^2/2)\frac{[\sqrt{1+4v^2} - (1+v^2)]^{1/2}}{2v^2 - 1 + \sqrt{1+4v^2}}\,. \tag{43}$$

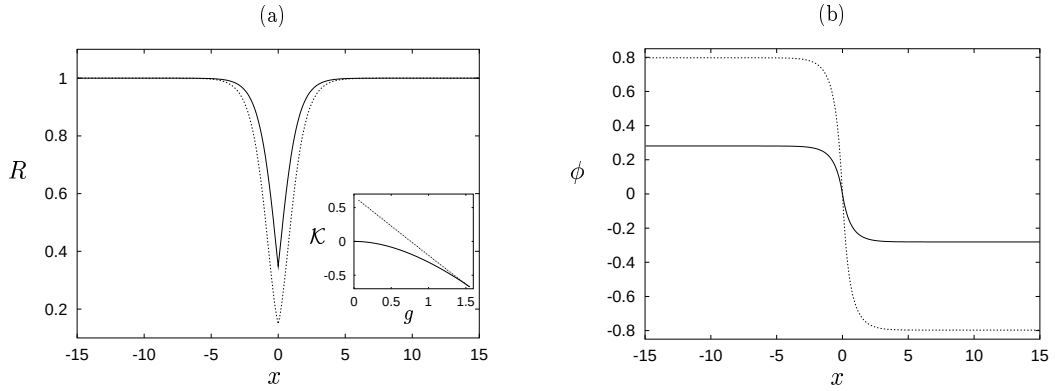

Fig. 8. (a) Modulus R of the stable (—) and unstable (- - -) stationary solutions of equation (32) (see equation (40)) for $g = 1.250$ and $v = 0.5$; insert, energy functional $\mathcal{K}$ of the stationary solutions versus g for $v = 0.5$ (see equation (28)); lower branch: energetically stable branch, upper branch: energetically unstable branch. The bifurcation occurs at $g = 1.5514$ (b) Phase ϕ of the stable (—) and unstable (- - -) stationary solutions (see equation (41)), same conditions as in (a).

The two stationary solutions of (32) corresponding to $\xi_+(g) > \xi_c$ and $\xi_-(g) < \xi_c$ obtained by inverting (42) for $g < g_c$ thus disappear, merging in a saddle-node bifurcation at a critical strength g_c. Note that the bifurcation can also be obtained by varying v and keeping g constant. In the following, the strength g of the delta function is used as the control parameter of our system, keeping v constant.

Fig. 8a shows the energetically unstable and stable solutions ($\mathcal{K}(\xi_-(g)) > \mathcal{K}(\xi_+(g))$) . The bifurcation diagram corresponding to the energy $\mathcal{K}$ (see equation (28)) is also displayed on the figure as an insert. In fig. 8b, note that the phase $\phi_\xi(x)$, as defined in equation (41), differs from that considered in [54] by an (x-independent) constant. The phase in [54] is set to 0 at $x = +\infty$, whereas (41) is antisymmetric in x. This difference is unimportant because equations (34) and (35) are invariant under the constant phase shift

$$\phi(x) \mapsto \phi(x) + \varphi\,. \tag{44}$$

4.2 General formulation

In this section we define and test the numerical tools needed to obtain the stationary solutions of the NLSE.

Consider the following action functional associated with the NLSE

$$\mathcal{A} = \int d\tilde{t} \left\{ \int d\tilde{\mathbf{x}} \frac{i}{2} \left(\overline{\psi} \frac{\partial \psi}{\partial \tilde{t}} - \psi \frac{\partial \overline{\psi}}{\partial \tilde{t}} \right) - \mathcal{F} \right\}, \tag{45}$$

where ψ is a complex field, $\overline{\psi}$ its conjugate and $\mathcal{F}$ is the energy of the system. Here, $\mathbf{x}$ and $\tilde{t}$ correspond to nondimensionalized space and time variables respectively.

The Euler-Lagrange equation corresponding to (45) leads to the NLSE in terms of the functional $\mathcal{F}$

$$\frac{\partial \psi}{\partial \tilde{t}} = -i \frac{\delta \mathcal{F}}{\delta \overline{\psi}}. \tag{46}$$

This equation obviously has stationary solution ψ_S if $\delta\mathcal{F}/\delta\psi|_{\psi=\psi_S} = 0$. Thus, stationary solutions of (46) are extrema of $\mathcal{F}$. In general, we are looking for an extremum of an energy functional $\mathcal{E}$ under some constraint $\mathcal{Q}[\psi] = cst$. The usual Lagrange multiplier trick consists in introducing a control parameter ν and, rather than solving for extrema of $\mathcal{E}[\psi]$, searching for extrema of the new functional $\mathcal{F}[\psi] = \mathcal{E}[\psi] - \nu\mathcal{Q}[\psi]$. We thus solve for

$$\left. \frac{\delta \mathcal{F}}{\delta \psi} \right|_{\nu=\text{cst.}} = 0. \tag{47}$$

We now turn to the precise definitions, corresponding to the two systems considered in this section : superflows and Bose-Einstein condensates.

4.2.1 Superflows

In the problem of a superflow past an obstacle, $\mathcal{E}$ is the hydrodynamic energy and $\nu \equiv \vec{U}$ is the flow velocity with respect to the obstacle [14,16]. This implies that $\mathcal{Q} \equiv \vec{\mathcal{P}}$ is the flow momentum. Functionals $\mathcal{F}$, $\mathcal{E}$ and $\vec{\mathcal{P}}$ are given by the expressions

$$\mathcal{F} = \mathcal{E} - \vec{\mathcal{P}} \cdot \vec{U} \tag{48}$$

$$\mathcal{E} = c^2 \int d^3x \left([-1 + V(\vec{x})]|\psi|^2 + \frac{1}{2}|\psi|^4 + \xi^2 |\nabla\psi|^2 \right) \tag{49}$$

$$\vec{\mathcal{P}} = \sqrt{2} c \xi \int d^3x \frac{i}{2} \left(\psi \nabla \overline{\psi} - \overline{\psi} \nabla \psi \right). \tag{50}$$

Here, c and ξ are the physical parameters characterizing the superfluid. They correspond to the speed of sound (c) for a fluid with mean density $\rho_0 = 1$, and to the coherence length (ξ). The potential $V(\vec{x}) = (V_o/2)(\tanh[4(r - D/2)/\Delta] - 1)$ is used to represent a cylindrical obstacle of diameter D. The computations are performed with $V_o = 10$ and $\Delta = \xi$ for which the density $|\psi| \sim 0$ in the disk. The NLSE reads

$$\frac{\partial \psi}{\partial t} = -\frac{i}{\sqrt{2}c\xi}\frac{\delta \mathcal{F}}{\delta \overline{\psi}} = i\frac{c}{\sqrt{2}\xi}\left([1 - V(\vec{x})]\psi - |\psi|^2\psi + \xi^2\nabla^2\psi\right) + \vec{U}\cdot\nabla\psi. \quad (51)$$

We will be interested in the solutions of $\delta\mathcal{F}/\delta\overline{\psi} = 0$, for a given value of $\vec{U}$. According to equation (47), these solutions are extrema of $\mathcal{E}$ at constant momentum $\vec{\mathcal{P}}$.

4.2.2 Bose-Einstein condensates

We consider a condensate of $\mathcal{N}$ particles of mass m and effective scattering length a in a radial confining harmonic potential $V(r) = m\omega^2 r^2/2$ [17]. Quantities are rescaled by the natural quantum harmonic oscillator units of time $\tau_0 = 1/\omega$ and length $L_0 = \sqrt{\hbar/m\omega}$, thus obtaining the nondimensionalized variables $\tilde{t} = t/\tau_0$, $\tilde{\mathbf{x}} = \mathbf{x}/L_0$ and $\tilde{a} = 4\pi a/L_0$. The control parameter ν becomes in this context the chemical potential μ. The total number of particles in the condensate is therefore given by $\mathcal{Q} \equiv \mathcal{N}$. Functionals $\mathcal{F}$, $\mathcal{E}$ and $\mathcal{N}$ are given, in terms of rescaled variables, by

$$\mathcal{F} = \mathcal{E} - \mu\mathcal{N} \quad (52)$$

$$\mathcal{E} = \int d^3\tilde{\mathbf{x}}\left(\frac{1}{2}|\nabla_{\tilde{\mathbf{x}}}\psi|^2 + V(\tilde{\mathbf{x}})|\psi|^2 + \frac{\tilde{a}}{2}|\psi|^4\right) \quad (53)$$

$$\mathcal{N} = \int d^3\tilde{\mathbf{x}}|\psi|^2. \quad (54)$$

Two different situations are possible, depending on the sign of the (rescaled) effective scattering length $\tilde{a}$. When $\tilde{a}$ is positive the particles interact repulsively. A negative $\tilde{a}$ corresponds to an attractive interaction. The dynamical equation is

$$\frac{\partial \psi}{\partial \tilde{t}} = -i\frac{\delta \mathcal{F}}{\delta \overline{\psi}} = i\left[\frac{1}{2}\nabla^2_{\tilde{\mathbf{x}}}\psi - \frac{1}{2}|\tilde{\mathbf{x}}|^2\psi - \left(\tilde{a}|\psi|^2 - \mu\right)\psi\right]. \quad (55)$$

We will be interested in the solutions of $\delta\mathcal{F}/\delta\overline{\psi} = 0$, for a given value of μ. According to equation (47), these solutions are extrema of $\mathcal{E}$ at constant particle number $\mathcal{N}$.

4.3 Branch following methods

When the extremum of $\mathcal{F}$ is a local *minimum*, the stationary solution ψ_S of (51) can be reached by a relaxation method. If the extremum is not a minimum, Newton's iterative method is used to solve for ψ_S.

4.3.1 Relaxation method

In what remains of this section, we will write the NLSE under the following generic form, which is valid for both the Bose-Einstein condensates and the superflow past an obstacle:

$$\frac{\partial \psi}{\partial t} = -i\frac{\delta \mathcal{F}}{\delta \overline{\psi}} = i\left(\alpha \nabla^2 \psi + [\Omega - V(\vec{x})]\,\psi - \beta|\psi|^2\psi\right) + \vec{U}\cdot\nabla\psi. \tag{56}$$

When the extremum of $\mathcal{F}$ is a local *minimum*, the stationary solution ψ_S of (56) can be reached by integrating to relaxation the associated real Ginzburg-Landau equation (RGLE)

$$\frac{\partial \psi}{\partial t} = -\frac{\delta \mathcal{F}}{\delta \overline{\psi}} = \alpha \nabla^2 \psi + [\Omega - V(\vec{x})]\,\psi - \beta|\psi|^2\psi - i\vec{U}\cdot\nabla\psi. \tag{57}$$

Indeed, (56) and (57) have the same stationary solutions.

In our numerical computations, equation (57) is integrated to convergence by using the Forward-Euler/Backwards-Euler time stepping scheme

$$\psi(t+\sigma) = \Theta^{-1}\left[\left(1 - i\,\sigma\,\vec{U}\cdot\nabla\right) + \sigma\,\left([\Omega - V(\vec{x})] - \beta|\psi(t)|^2\right)\right]\psi(t) \tag{58}$$

with

$$\Theta = \left[1 - \sigma\,\alpha\nabla^2\right]. \tag{59}$$

The advantage of this method is that it converges to the stationary solution of (56) independently of the time step σ.

4.3.2 Newton's method

We use Newton's method [58] to find unstable stationary solutions of the RGLE.

In order to work with a well-conditioned system [59], we search for the fixed points of (58). These can be found as the roots of

$$f(\psi) = \Theta^{-1}\left[\left(1 - i\,\sigma\,\vec{U}\cdot\nabla\right) + \sigma\,\left([\Omega - V(\vec{x})] - \beta|\psi(t)|^2\right)\right]\psi(t) - \psi(t), \tag{60}$$

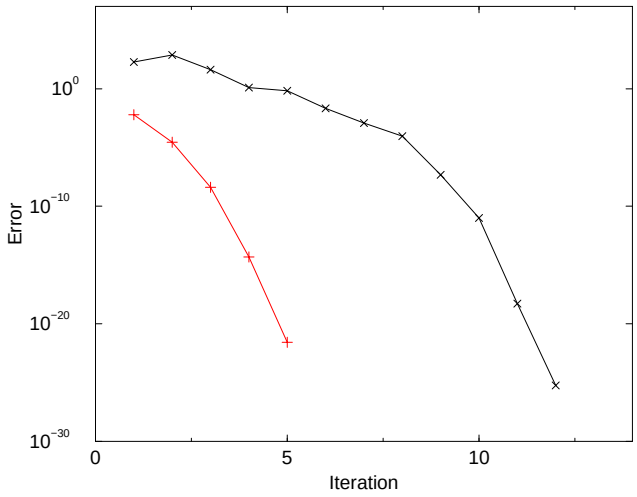

Fig. 9. Two typical examples of the Newton method convergence towards the solution of equation (60) for the problem of a superflow past a cylinder with $\xi/D = 1/10$ and a field $\psi_{(j)}$ discretized into $n = 128 \times 64 = 8190$ collocation points. The error measure is given by $\sum_{j=1}^{n} f_{(j)}^2(\psi)/n$. The convergence is faster than exponential, as expected for a Newton method.

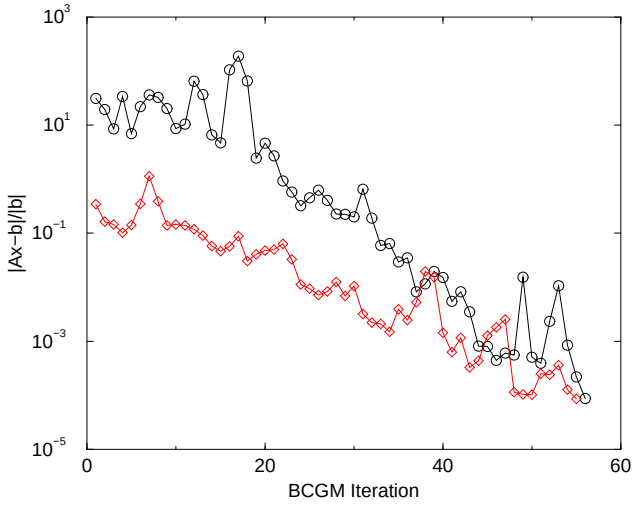

Fig. 10. Two typical examples of a bi-conjugate gradient method convergence corresponding to the case shown on figure 9. The convergence of the relative error achieved for the $\mathbf{x}$ solution of $\mathbf{Ax{=}b}$ is given by $|\mathbf{Ax}{-}\mathbf{b}|/|\mathbf{b}|$, where $\mathbf{A}{=}\,[df_{(j)}/d\psi_{(k)}]$, $\mathbf{b}{=}\,-f_{(j)}(\psi)$ and $\mathbf{x}{=}\,\delta\psi_{(k)}$.

where Θ^{-1} was already introduced in equation (58).

We denote by $\psi_{(j)}$ the value of the field ψ at the j-th collocation point. The roots of $f(\psi)$ are found by solving the linear problem

$$\sum_k \left[\frac{df_{(j)}}{d\psi_{(k)}}\right] \delta\psi_{(k)} = -f_{(j)}(\psi). \tag{61}$$

for $\delta\psi$ and then incrementing ψ by

$$\psi_{(j)} = \psi_{(j)} + \delta\psi_{(j)} \tag{62}$$

and iterating the Newton process (61)-(62) to convergence.

The solution to (61) is obtained by an iterative bi-conjugate gradient method either BCGM [60] or BiCGSTAB [61]. These methods require only the ability to act repeatedly with $[df_{(j)}/d\psi_{(k)}]$ on an arbitrary field φ to obtain an approximative solution of (61). Note that since the convergence of the time step (58) does not depend on σ, the roots found through this Newton iteration are also independent of σ. Therefore, σ becomes a free parameter that can be used to adjust the pre-conditioning of the system in order to optimize the convergence of the BCGM [59].

4.3.3 Implementation

We use standard Fourier pseudo spectral methods [38]. Typical convergences of the Newton and bi-conjugate gradient iterations are shown in figures 9 and 10.

In the case of the radially symmetric Bose condensate, $\psi(r,\tilde{t})$ is expanded as $\psi(r,\tilde{t}) = \sum_{n=0}^{N_R/2} \hat{\psi}_{2n}(\tilde{t}) T_{2n}(r/R)$, where T_n is the n-th order Chebychev polynomial and $\hat{\psi}_{N_R}$ is fixed to satisfy the boundary condition $\psi(R,\tilde{t}) = 0$.

The NLSE is integrated in time by a fractional step (operator-splitting) method [62].

4.4 Stability of a superflow around a cylinder

In this section, following references [14–16], we investigate the stationary stable and unstable (nucleation) solutions of the NLSE describing the superflow around a cylinder, using the numerical methods developed in section 4.3. We study a disc of diameter D, moving at speed $\vec{U}$ in a two-dimensional (2D) superfluid at rest. The NLSE (51) can be mapped into two hydrodynamical equations by applying Madelung's transformation [1,35]:

$$\psi = \sqrt{\rho} \exp\left(\frac{i\phi}{\sqrt{2}c\xi}\right). \tag{63}$$

The real and imaginary parts of the NLSE produce for a fluid of density ρ and velocity

$$\vec{v} = \nabla\phi - \vec{U}, \tag{64}$$

the following equations of motion

$$\frac{\partial \rho}{\partial t} + \nabla\left(\rho \vec{v}\right) = 0 \qquad (65)$$

$$\left[\frac{\partial \phi}{\partial t} - \vec{U}\cdot\nabla\phi\right] + \frac{1}{2}(\nabla\phi)^2 + c^2[\rho - (1 - V(\vec{x}))] - c^2\xi^2\frac{\nabla^2\sqrt{\rho}}{\sqrt{\rho}} = 0. \qquad (66)$$

In the coordinate system $\vec{x}$ that follows the obstacle, these equations correspond to the continuity equation and to the Bernoulli equation [4] (with a supplementary *quantum pressure* term $c^2\xi^2\nabla^2\sqrt{\rho}/\sqrt{\rho}$) for an isentropic, compressible and irrotational flow. Note that, in the limit where $\xi/D \to 0$, the quantum pressure term vanishes and we recover the system of equations describing an Eulerian flow.

4.4.1 Bifurcation diagram and scaling in 2D

In this section, varying the ratio of the coherence length ξ to the cylinder diameter D, we obtain scaling laws in the $\xi/D \to 0$ limit.

Bifurcation diagram

We present results for $\xi/D = 1/10$ which are representative of all ratios we computed. The functional $\mathcal{E}$ and energy $\mathcal{F}$ of the stationary solutions are shown in Fig. 11 as a function of the Mach number ($M = |\vec{U}|/c$). The stable branch (a) disappears with the unstable solution (c) at a saddle-node bifurcation when $M = M^c \approx 0.4286$. The energy $\mathcal{F}$ has a cusp at the bifurcation point, which is the generic behavior for a Hamiltonian saddle-node bifurcation, as described in section 4.5.1. There are no stationary solutions beyond this point. When $M^{\rm pf} \approx 0.4282$, the unstable symmetric branch (c) bifurcates at a pitchfork to a pair of asymmetric branches (b). Their nucleation energy barrier is given by $(\mathcal{F}_{b'} - \mathcal{F}_{a'})$ which is roughly half of the barrier for the symmetric branch $(\mathcal{F}_{c'} - \mathcal{F}_{a'})$.

We can relate branches in Fig. 11 to the presence of vortices in the solution. When $M^{\rm n} \leq M \leq M^c$, solutions are irrotational ($M^{\rm n} \sim 0.405$ as indicated in Fig. 11). For $M \leq M^{\rm n}$ the stable branch (a) remains irrotational (Fig. 12A) while the unstable branch (b) corresponds to a one vortex solution (Fig. 12B) and the unstable branch (c), to a two vortex solution (Fig. 12C). The distance between the vortices and the obstacle in branches (b) and (c) increases when M is decreased. Branch (c) is precisely the situation described in [63]. Furthermore, the value $M^c \approx 0.4286$ is close to the predicted value $\sqrt{2/11}$. Figure 12D shows the result of integrating the NLSE forward in time with, as initial condition, a slightly perturbed unstable symmetric stationary state (Fig. 12C). The perturbation drives the system over the nucleation barrier

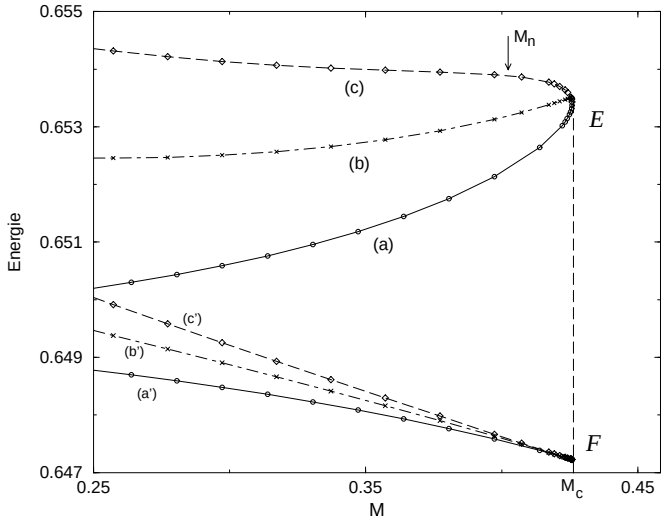

Fig. 11. Plot of the energy ($\mathcal{F}$), and functional ($\mathcal{E}$) versus Mach number ($M = |\vec{U}|/c$), with $D = 10\xi$. Stable state (a). Nucleation solutions: asymmetric branch (b) and symmetric branch (c). The diagram shows a saddle-node and a pitchfork bifurcation. The point where vortices cross the surface of the disc (see Fig. 12) is labelled by $M_{\rm n}$. The total fluid momentum is given by $-d\mathcal{F}/dU$ (see text).

and cycles it, after the emission of two vortices, back to a stationary stable solution. This shows that the branch (c) corresponds to hyperbolic fixed points of NLSE.

Figures 12E,F show the phase of the field at the surface of the disc ($r = D/2$ and $\theta \in [0, 2\pi]$) for four different flow speeds. In both unstable branches, 2π-discontinuities, a diagnostic of vortex crossing, appear between $M = 0.40$ and $M = 0.41$.

Scaling laws

We now characterize the dependence on ξ/D of the main features of the bifurcation diagram. When ξ/D is decreased, M^c and $M^{\rm pf}$ become indistinguishable. In the limit where $\xi/D = 0$, the critical Mach number M^c will be that of an Eulerian flow $M^c_{\rm Euler}$.

Figure 13 shows the convergence of M^c to the Eulerian critical velocity. This convergence can be characterized by fitting the polynomial law $M^c = K_1(\xi/D)^{K_2} + M^c_{\rm Euler}$ to $M^c(\xi/D)$. This fit is shown on Fig. 13 as a dotted line, yielding $K_1 = 0.322$, $K_2 = 0.615$ and $M^c_{\rm Euler} = 0.35$.

Dynamical solutions

The stationary solutions obtained in the above subsection provide adequate

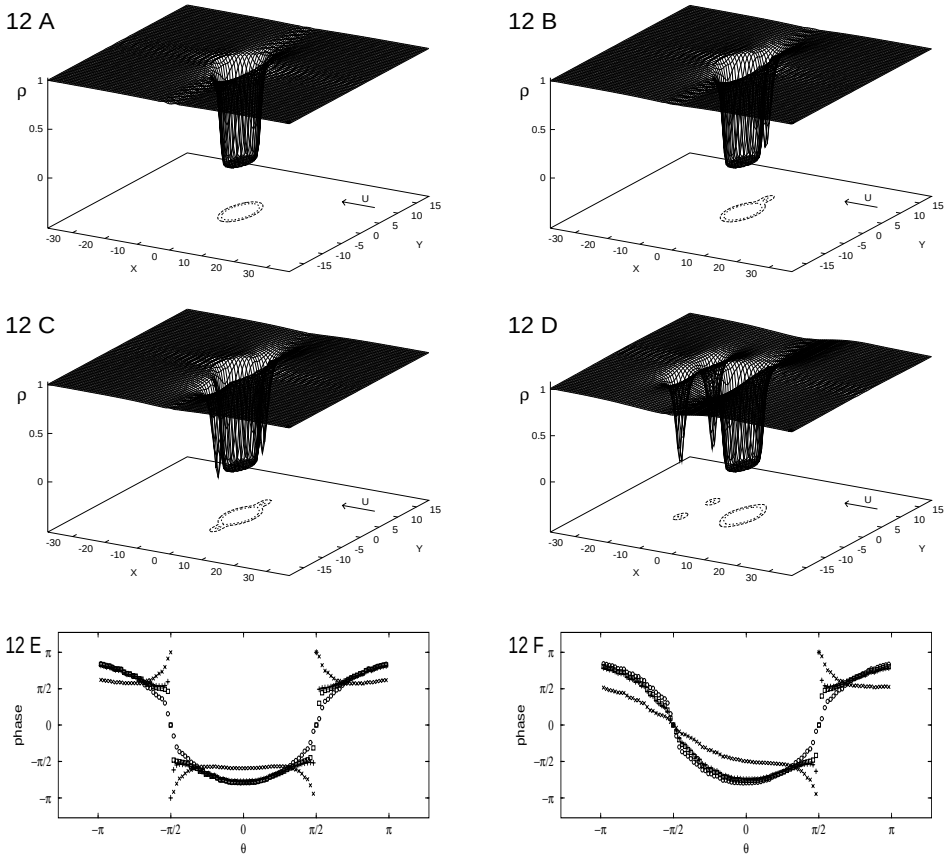

Fig. 12. Stationary states : stable state (A), one vortex unstable state (B), two vortex unstable state (C). The surface indicates the fluid density around the cylinder ($M = 0.24, \xi/D = 0.1$). Figure (D) shows the result of the NLSE integration, starting from a slightly perturbed stationary (C) state. Figures (E) and (F) display the phase of the complex field ψ at the surface of the cylinder versus the polar angle θ. Symmetric branch (E), asymmetric branch (F). $M = 0.4286$ ($\circ$), $M = 0.41$ ($\Box$), $M = 0.40$ ($+$), $M = 0.30$ ($\times$). The crossing out of the vortex produces a phase discontinuity at $M^{\rm n} \sim 0.405$.

initial data for the study of dynamical solutions. Indeed, after a small perturbation, their integration in time will generate a dynamical evolution with very small acoustic emission. Therefore, this procedure is an efficient way to initialize vortical dynamics in a controlled manner.

Starting from a two-vortex unstable stationary solution at a supercritical Mach number $M^c = 0.9$, the evolution of the NLSE time integration shows a clearly periodic emission of vortex pairs (see Fig. 12). This emission conserves total circulation.

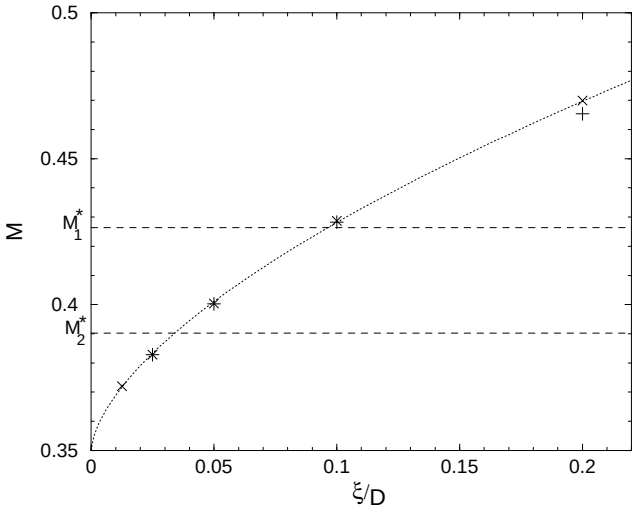

Fig. 13. Saddle-node bifurcation Mach number M^c (+) and pitchfork bifurcation Mach number $M^{\rm pf}$ ($\times$), as a function of ξ/D. The dotted curve corresponds to a fit to the polynomial law $M^c = K_1(\xi/D)^{K_2} + M^c_{\rm Euler}$ with $K_1 = 0.322$, $K_2 = 0.615$ and $M^c_{\rm Euler} = 0.35$.

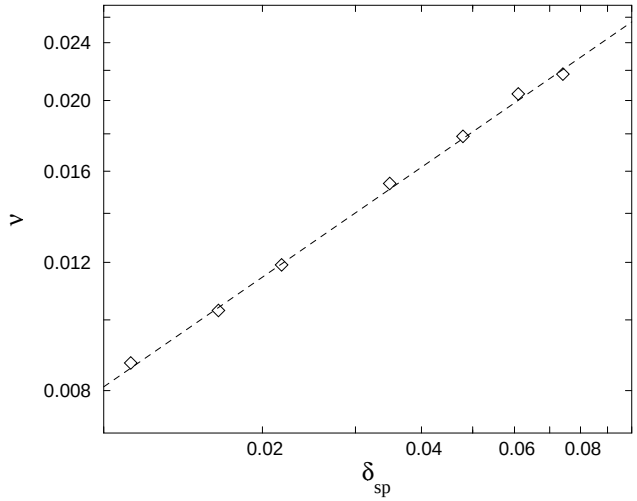

Fig. 14. Vortex emission frequency as a function of $\delta_{\rm sp} = (M - M^c)/M^c \ll 1$ (with $M^c = 0.3817$), for a symmetric wake and $\xi/D = 1/20$. The dashed line shows a fit of a polynomial $\nu = K_1\delta_{\rm sp}^{1/2}$ with $K_1 = 0.081$. The obtained $\delta_{\rm sp}^{1/2}$ law for the frequency is equivalent to that expected for a dissipative system.

We have studied the behavior of the frequency of vortex emission close to the bifurcation for these symmetric wakes with different supercritical velocities (characterized by $\delta_{\rm sp} = (M - M^c)/M^c = -\delta > 0$). Our results, plotted on Fig. 14, are consistent with a $\delta_{\rm sp}^{1/2}$ scaling.

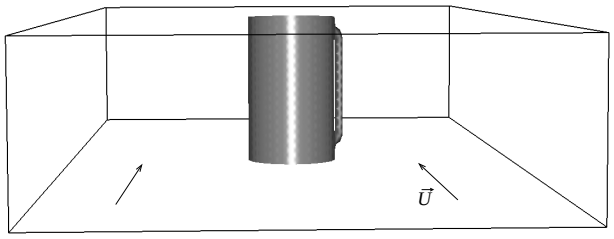

Fig. 15. Initial condition of a vortex pinned to the cylinder generated by equation (67). The surface $|\psi_{3D}| = 0.5$ is shown for $\xi/D = 0.025$, $|\vec{U}|/c = 0.26$ and $\Delta_z = 2\sqrt{2}\xi$ in the $[L_x \times L_y \times L_z]$ periodicity box ($L_x/D = 2.4\sqrt{2}\pi$, $L_y/D = 1.2\sqrt{2}\pi$ and $L_z/D = 0.4\sqrt{2}\pi$).

4.4.2 Subcriticality and vortex-stretching in 3D

In this section, using a 3D version of our code to integrate the NLSE, we study 3D instabilities of the basic 2D superflow.

Preparation method

We used the 2D laminar stationary solution $\psi_{0V}(x, y)$ (corresponding to branch (a) of the preceding section) and the one-vortex unstable stationary solution $\psi_{1V}(x, y)$ (branch (b)) to construct the 3D initial condition

$$\psi_{3D}(x, y, z) = f_I(z)\psi_{1V}(x, y) + [1 - f_I(z)]\psi_{0V}(x, y). \tag{67}$$

The function $f_I(z)$, defined by

$$f_I(z) = (\tanh[(z - z_1)/\Delta_z] - \tanh[(z - z_2)/\Delta_z])/2,$$

takes the value 1 for $z_1 \leq z \leq z_2$ and 0 elsewhere, with Δ_z an adaptation length.

Figure 15 represents a 3D initial data prepared with this method for $\xi/D = 0.025$, $|\vec{U}|/c = 0.26$ and $\Delta_z = 2\sqrt{2}\xi$ in the $[L_x \times L_y \times L_z]$ periodicity box ($L_x/D = 2.4\sqrt{2}\pi$, $L_y/D = 1.2\sqrt{2}\pi$ and $L_z/D = 0.4\sqrt{2}\pi$). The surface $|\psi_{3D}| = 0.5$ defines the cylindrical surface and the initial condition vortex line, with both ends pinned to the right side of the cylinder.

Short time dynamics

Starting from the initial condition (67), the evolution of the NLSE time integration shows different short-time and long-time dynamics.

During the short-time dynamics, the initial pinned vortex line rapidly contracts, evolving through a decreasing number of half-ring-like loops, down to a single quasi-stationary half-ring (see Figs. 16a, 16b, 16c). This evolution takes place mainly on the plane perpendicular to the flow, provided that the

initial vortex is long enough to contract to a quasi-stationary half-ring as shown on Fig. 16c. Otherwise, the vortex line collapses against the cylinder while moving upstream.

Note that this quasi-stationary half-ring has been used by Varoquaux [64,65] to estimate the nucleation barrier in a 3D experiment.

The dynamics of the half-ring situation (Fig. 16c) is very slow and can be shown to be close to a stationary field. Indeed, the local flow velocity v in an Eulerian flow around a cylindrical obstacle is known to vary from $v = |\vec{U}|$ at infinity to $v = 2|\vec{U}|$ at both sides of its surface. Moreover, the diameter d of a stationary vortex ring in an infinite Eulerian flow with no obstacle is given by [1]:

$$|\vec{U}|/c = (\sqrt{2}\xi/d)\left[\ln\left(4d/\xi\right) - K\right], \tag{68}$$

where $|\vec{U}|$ is the flow velocity at infinity and the vortex core model constant $K \sim 1$ is obtained by fitting the numerical results in [66]. Therefore, for the values used on Figs. 16, we expect that local velocities range from $v = 0.25$ to $v = 2 \times 0.25$. Equation (68) thus implies that the diameter of an hypothetical stationary half-ring should be bounded by $d(v = |\vec{U}| = 0.25) = 18.8\xi$ and $d(v = 2|\vec{U}| = 0.5) = 6.3\xi$. The diameter $d \approx 9\xi$ measured on the half-ring observed on Fig. 16c is consistent with its quasi-stationary behavior. Similarly the diameter of the half-ring shown on Fig. 18 $d \approx 7.6\xi$ is also found to be between the corresponding bounds $d(0.35) = 11.4\xi$ and $d(2 \times 0.35) = 3\xi$.

Vortex stretching as a subcritical drag mechanism

A small perturbation over the half-ring solution can drive the system into two opposite situations where the half-ring either starts moving upstream or downstream.

When driven upstream, the half-ring eventually collapses against the cylinder, dissipating its energy as sound waves. Otherwise, the vortex loop is stretched while the pinning points move towards the back of the cylinder. Figures 17 show the long-time dynamics for a stretching case with $\xi/D = 1/40$ and $|\vec{U}|/c = 0.25$ starting from Fig. 16c. Figure 19 shows a later situation for $\xi/D = 1/20$ and $|\vec{U}|/c = 0.35$ starting from Fig. 18. As the vortex loop grows, its backmost part remains oblique to the flow. This vortex stretching mechanism consumes energy, thus generating drag. It could be responsible for the appearance of drag in experimental superflows if fluctuations are strong enough to nucleate the initial vortex loop (which is imposed extrinsically in our numerical system). Note that it takes place for 2D subcritical velocities.

Figure 20 displays several numerical and experimental [67] critical Mach numbers (V_c/C) with respect to D/ξ, which seem to follow a (-1) slope in a

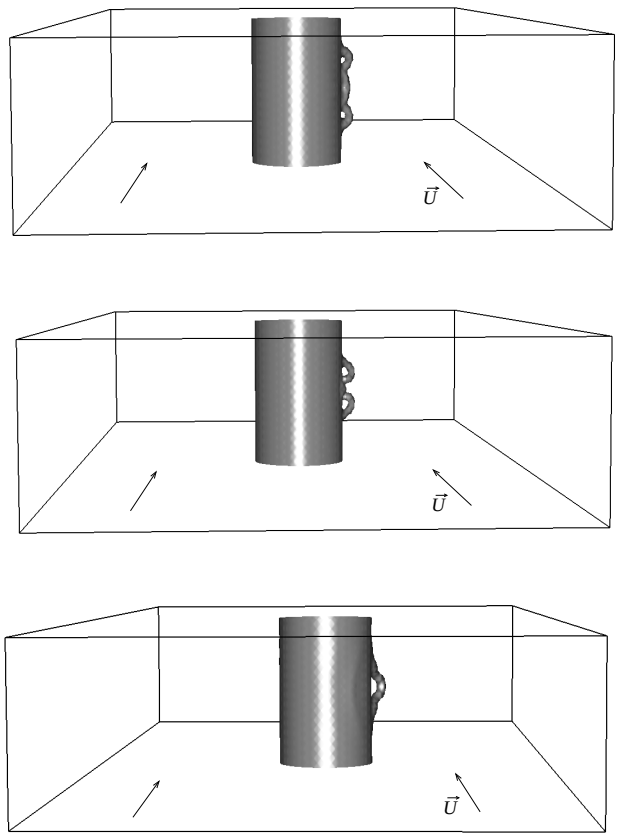

Fig. 16. Short-time dynamics for $\xi/D = 1/40$ and $|\vec{U}|/c = 0.25$ starting from Fig. 15: A ($t = 5\xi/c$), B($t = 10\xi/c$) and C($t = 15\xi/c$). The contraction of the initial vortex line occurs in the plane perpendicular to the flow. The half-rings have a diameter compatible with that of a quasi-stationary half-ring (see text).

log-log plot. The squares stand for our numerical stretching cases while the crosses correspond to non-stretching cases. There is a frontier between the 3D numerical dissipative and non-dissipative cases [16]. For $1/30 < \xi/D < 1/20$, the frontier corresponds to the expression $R_s = 5.5$ with

$$R_s \equiv |\vec{U}|D/c\xi = MD/\xi. \tag{69}$$

This superfluid 'Reynolds' number is defined in the same way as the standard (viscous) Reynolds number $Re \equiv |\vec{U}|D/\nu$ (with ν the kinematic viscosity). It has been shown, in the superfluid turbulent ($R_s \gg 1$) regime, that R_s is equivalent to the standard (viscous) Reynolds number Re [12,11,13]. Note that, for a Bose condensate of particles of mass m, the quantum of velocity circulation around a vortex, $\Gamma = 2\pi\sqrt{2}c\xi$, has the Onsager-Feynman value $\Gamma = h/m$ (h is Planck's constant) and the same physical dimensions L^2T^{-1} as ν.

The value of R_s divides the space of parameters into a laminar flow zone and

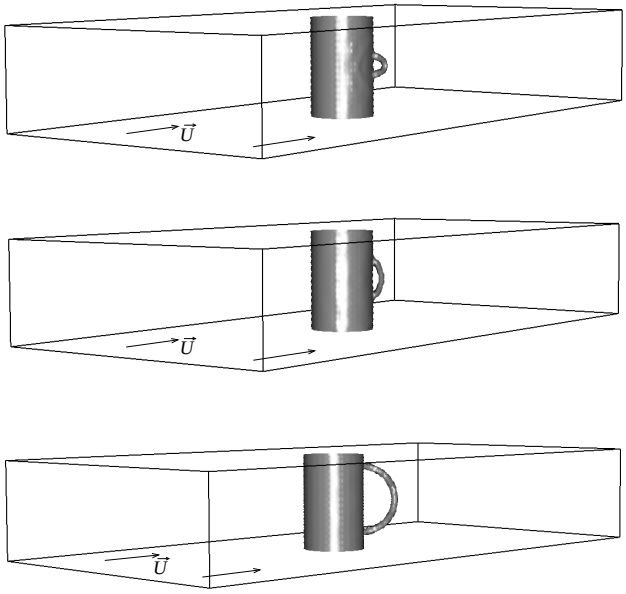

Fig. 17. Long-time dynamics for $\xi/D = 1/40$ and $|\vec{U}|/c = 0.25$ starting from Fig. 16c. The half-ring moves downstream while growing.

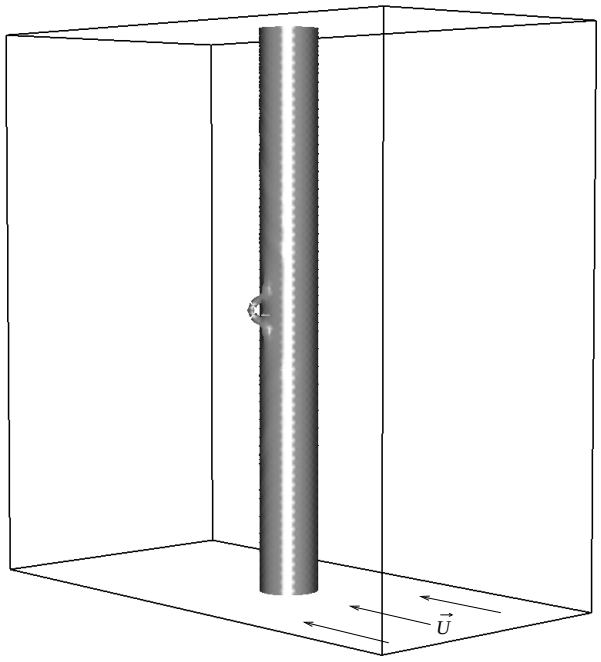

Fig. 18. Quasi-nucleation solution for $|\vec{U}|/c = 0.35$ and $\xi/D = 1/20$ at time $t = 15\xi/c$.

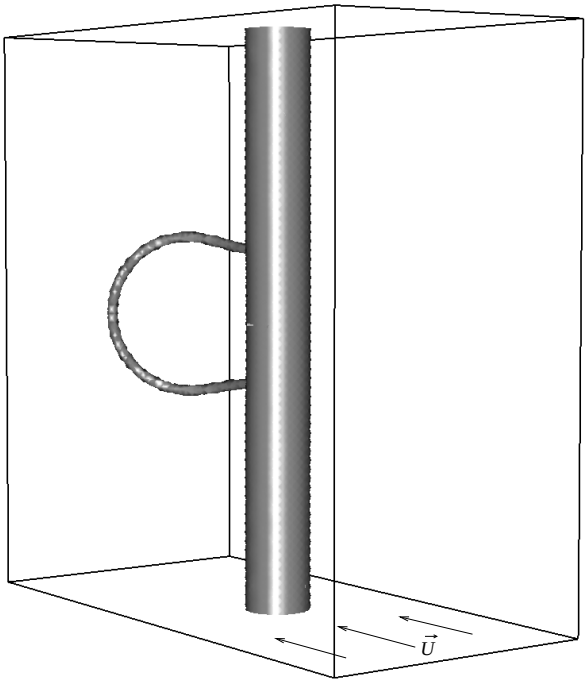

Fig. 19. Vortex stretching at $t = 150\xi/c$ with $|\vec{U}|/c = 0.35$ and $\xi/D = 1/20$. The vortex line is oblique to the flow.

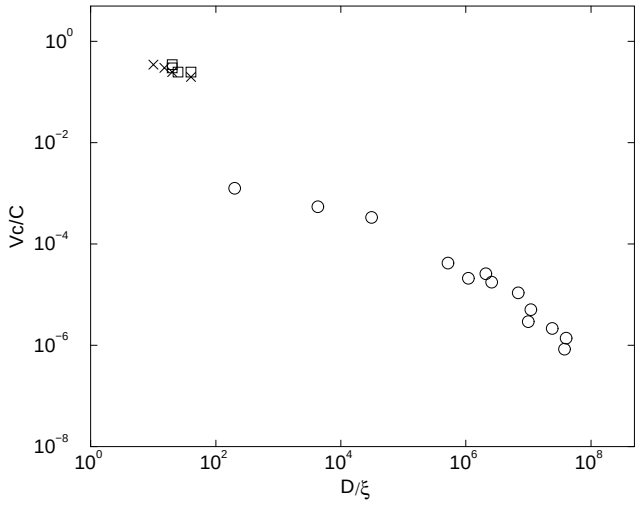

Fig. 20. Critical Mach number V_c/C versus scale ratio of numerical and experimental data D/ξ. Circles correspond to several experiments from [67]. Squares stand for our numerical stretching cases while crosses correspond to non-stretching cases [16]. Note the wide difference in values of parameter $\xi/D \simeq 10^{-1}$ for our numerics (corresponding to current experiments in BEC) and ξ/D down to 10^{-8} older experiments in liquid Helium).

a recirculating flow zone, very much like in the problem of a circular disc in a viscous fluid in which this frontier is also found to be around $Re \sim 5$. Thus, there seems to exist some degree of universality between viscous normal fluids and superfluids modeled by NLSE as discussed in [12,11,13]. In the context of superfluid ^{4}He flow, the experimental critical velocity is known to depend strongly on the system's characteristic size D. It is often found to be well below the Landau value (based on the velocity of roton excitation) except for experiments in which ions are dragged in liquid helium. Feynman's alternative critical velocity criterion $R_s \sim \log(D/\xi)$ is based on the energy needed to form vortex lines. It produces better estimates for various experimental settings, but does not describe the vortex nucleation mechanism [1].

In a recent experiment, Raman *et al.* have studied dissipation in a Bose-Einstein condensed gas by moving a blue detuned laser beam through the condensate at different velocities [68]. In their inhomogeneous condensate, they observed a critical Mach number for the onset of dissipation $M^c_{2D}/1.6$.

Our computations were performed for values of ξ/D comparable to those in Bose-Einstein condensed gas experiments. They demonstrate the possibility of a subcritical drag mechanism, based on 3D vortex stretching. It would be very interesting to determine experimentally the dependence of the critical Mach number on the parameter ξ/D and the nature (2D or 3D) of the excitations [16].

4.5 Stability of attractive Bose-Einstein condensates

In this section, following reference [17], we study condensates with attractive interactions which are known to be metastable in spatially localized systems, provided that the number of condensed particles is below a critical value $\mathcal{N}_c$ [7]. Various physical processes compete to determine the lifetime of attractive condensates. Among them one can distinguish macroscopic quantum tunneling (MQT) [69,70], inelastic two and three body collisions (ICO) [71,72] and thermally induced collapse (TIC) [70,73]. We compute the life-times, using both a variational Gaussian approximation and the exact numerical solution for the condensate wave-function.

4.5.1 Computations of stationary states

Gaussian approximation

A Gaussian approximation for the condensate density can be obtained analytically through the following procedure.

Inserting

$$\psi(r,\tilde{t}) = A(\tilde{t}) \exp\left(-r^2/2r_{\rm G}^2(\tilde{t}) + ib(\tilde{t})r^2\right) \tag{70}$$

into the action (45), where $\mathcal{F}$ is given by (52), yields a set of Euler-Lagrange equations for $r_{\rm G}(\tilde{t})$, $b(\tilde{t})$ and the (complex) amplitude $A(\tilde{t})$. The stationary solutions of the Euler-Lagrange equations produce the following values [74]:

$$\mathcal{N}(\mu) = \frac{4\sqrt{2\pi^3}\left(-8\mu + 3\sqrt{7+4\mu^2}\right)}{7|\tilde{a}|\left(-2\mu+\sqrt{7+4\mu^2}\right)^{3/2}}, \tag{71}$$

$$\mathcal{E} = \mathcal{N}(\mu)\left(-\mu + 3\sqrt{7+4\mu^2}\right)/7. \tag{72}$$

$\mathcal{N}$ is found to be maximal at $\mathcal{N}_c^G = 8\sqrt{2\pi^3}/|5^{5/4}\tilde{a}|$. The corresponding value of the chemical potential is $\mu = \mu_c^G = 1/2\sqrt{5}$.

Linearizing the Euler-Lagrange equations around the stationary solutions, yields the following expression for the eigenvalues [74]:

$$\lambda^2(\mu) = 8\mu^2 - 4\mu\sqrt{7+4\mu^2} + 2 \tag{73}$$

This qualitative behavior is the generic signature of a Hamiltonian saddle-node (HSN) bifurcation defined, at lowest order, by the normal form [75]

$$m_{eff}\ddot{Q} = \delta - \beta Q^2, \tag{74}$$

where $\delta = (1 - \mathcal{N}/\mathcal{N}_c)$ is the bifurcation parameter. The critical amplitude Q is related to the radius of the condensate [74]. We can relate the parameters β and m_{eff} to critical scaling laws, by defining the appropriate energy

$$\mathcal{E} = \mathcal{E}_0 + m_{\rm eff}\dot{Q}^2/2 - \delta\ Q + \beta Q^3/3 - \gamma\delta. \tag{75}$$

From (74) it is straightforward to derive, close to the critical point $\delta = 0$, the universal scaling laws

$$\mathcal{E}_\pm = \mathcal{E}_c - \mathcal{E}_l\delta \pm \mathcal{E}_\Delta\delta^{3/2}, \tag{76}$$

$$\lambda_\pm^2 = \pm\lambda_\Delta^2\delta^{1/2}, \tag{77}$$

where $\mathcal{E}_c = \mathcal{E}_0$, $\mathcal{E}_l = \gamma$, $\mathcal{E}_\Delta = 2/3\sqrt{\beta}$ and $\lambda_\Delta^2 = 2\sqrt{\beta}/m_{eff}$.

Numerical branch following

Using the branch-following method described in section 4.3, we have computed the exact stationary solutions of the NLSE. We use the following value $\tilde{a} =$

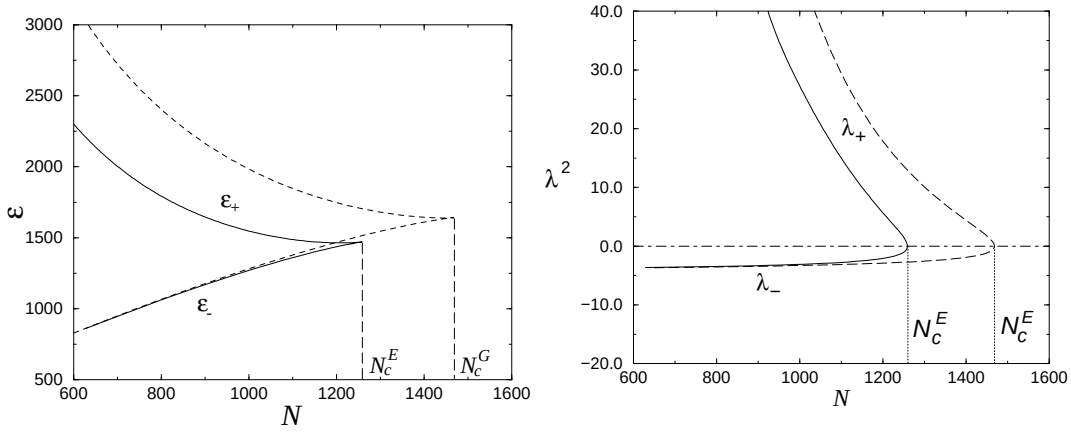

Fig. 21. Stationary solutions of the NLSE equation versus particle number $\mathcal{N}$. Left: value of the energy functional $\mathcal{E}_+$ on the stable (elliptic) branch and $\mathcal{E}_-$ on the unstable (hyperbolic) branch. Right: square of the bifurcating eigenvalue ($\lambda_\pm^2$); $|\lambda_-|$ is the energy of small excitations around the stable branch. Solid lines: exact solution of the NLSE equation. Dashed lines: Gaussian approximation.

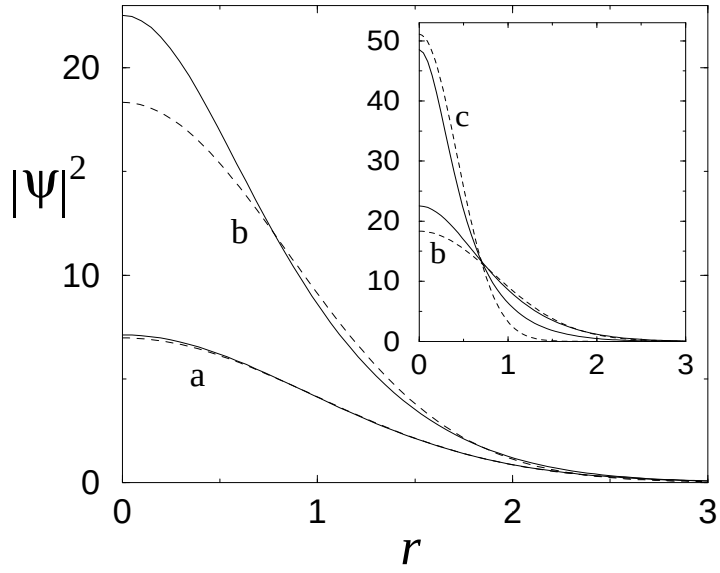

Fig. 22. Condensate density $|\psi|^2$ versus radius r, in reduced units (see text). Solid lines: exact solution of the NLSE equation. Dashed lines: Gaussian approximation. Stable (elliptic) solutions are shown for particle number $\mathcal{N} = 252$ (a) and $\mathcal{N} = 1132$ (b). (c) is the unstable (hyperbolic) solution for $\mathcal{N} = 1132$ (see insert).

-5.74×10^{-3}, that corresponds to experiments with ^{7}Li atoms in a radial trap [76,7].

As is apparent on Fig. 21, the exact critical $\mathcal{N}_c^E = 1258.5$ is smaller than the Gaussian value $\mathcal{N}_c^G = 1467.7$ [77,69]. The critical amplitudes corresponding to the Gaussian approximation can be computed from (71) and (72). One

finds $\mathcal{E}_c = 4\sqrt{2\pi^3}/|5^{3/4}\tilde{a}|$, $\mathcal{E}_\Delta = 64\sqrt{\pi^3}/|5^{9/4}\tilde{a}|$ and $\lambda_\Delta^2 = 4\sqrt{10}$. For the exact solutions, we obtain the critical amplitudes by performing fits on the data. One finds $\mathcal{E}_\Delta = 1340$ and $\lambda_\Delta^2 = 14.68$. Thus, the Gaussian approximation captures the bifurcation qualitatively, but with quantitative 17% error on N_c [77], 24% error on $\mathcal{E}_\Delta$ and 14% error on λ_Δ^2. Fig. 22 shows the physical origin of the quantitative errors in the Gaussian approximation. By inspection it is apparent that the exact solution is well approximated by a Gaussian only for small $\mathcal{N}$ on the stable (elliptic) branch.

4.5.2 Estimation of life-times

In this section, we estimate the decay rates due to thermally induced collapse, macroscopic quantum tunneling and inelastic collisions.

Thermally induced collapse

The thermally induced collapse (TIC) rate Γ_T is estimated using the formula [78]

$$\frac{\Gamma_T}{\omega} = \frac{|\lambda_+|}{2\pi} \exp\left[\frac{-\hbar\omega\,(\mathcal{E}_+ - \mathcal{E}_-)}{k_B T}\right] \tag{78}$$

where $\hbar\omega(\mathcal{E}_+ - \mathcal{E}_-)$ is the (dimensionalized) height of the nucleation energy barrier, T is the temperature of the condensate and k_B is the Boltzmann constant. Note that the prefactor characterizes the typical decay time which is controlled by the slowest part of the nucleation dynamics: the top-of-the-barrier saddle point eigenvalue λ_+. The behavior of Γ_T can be obtained directly from the universal saddle-node scaling laws (76) and (77). Thus the exponential factor and the prefactor vanish respectively as $\delta^{3/2}$ and $\delta^{1/4}$.

Macroscopic quantum tunneling

We estimate the MQT decay rate using an instanton technique that takes into account the semi classical trajectory giving the dominant contribution to the quantum action path integral [70,69]. This trajectory is approximated as the solution of

$$\frac{d^2 q(t)}{dt^2} = -\frac{d\Phi(q)}{dq}. \tag{79}$$

$\Phi(q)$ is a polynomial such that $-\Phi(q)$ reconstructs the Hamiltonian dynamics, and is determined by the relations

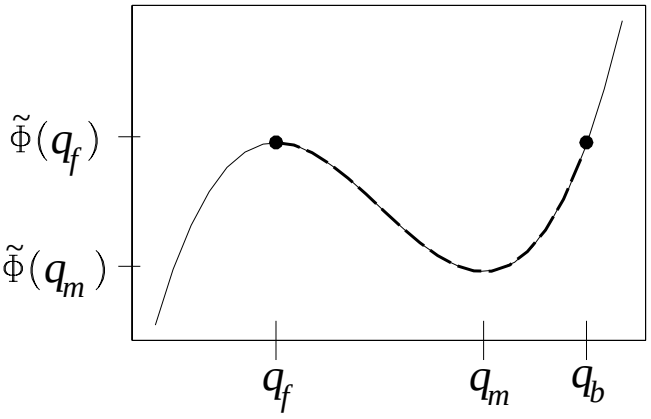

Fig. 23. The bounce trajectory is shown as dashes, above the potential $\Phi(q)$.

$$\Phi(q_m) = -\mathcal{E}_+ \tag{80}$$
$$\Phi(q_f) = -\mathcal{E}_- \tag{81}$$
$$\partial_q^2 \Phi(q_m) = |\lambda_+(\mathcal{N})| \tag{82}$$
$$\partial_q^2 \Phi(q_f) = -|\lambda_-(\mathcal{N})|. \tag{83}$$

The bounce trajectory is displayed on Fig. 23 (dashed line) above the potential $\Phi(q)$. The MQT rate is estimated as

$$\frac{\Gamma_Q}{\omega} = \sqrt{\frac{|\lambda_-|v_0^2}{4\pi}} \exp\left[\frac{-4}{\sqrt{2}} \int_{q_f}^{q_b} \sqrt{\Phi(q) - \Phi(q_f)} dq\right], \tag{84}$$

where v_0 is defined by the asymptotic form of the bounce trajectory $q(t)$ [70]: $q(\tau) \sim q_f + (v_0/|\lambda_-|) \exp[-|\lambda_-\tau|]$. Universal scaling laws can be derived close to criticality from (74), (76) and (77). The exponential factor in (84) follows the same scaling than $\sqrt{|\mathcal{E}_+ - \mathcal{E}_-|}dq$. It therefore vanishes as $\delta^{5/4}$. ¿From the asymptotic form of $q(t)$, dq follows the same law as $v_0/|\lambda_-|$. Thus $v_0 \sim \delta^{3/4}$ and the prefactor vanishes as $\delta^{7/8}$.

Inelastic collision

The inelastic collision rate (ICO) is estimated using the relation

$$\frac{d\mathcal{N}}{dt} = f_C(\mathcal{N}) \tag{85}$$

with

$$f_C(\mathcal{N}) = K \int |\psi|^4 d^3\tilde{\mathbf{x}} + L \int |\psi|^6 d^3\tilde{\mathbf{x}}, \tag{86}$$

where $K = 3.8 \times 10^{-4}\,\mathrm{s}^{-1}$ and $L = 2.6 \times 10^{-7}\,\mathrm{s}^{-1}$. The ICO rate can be evaluated from the stable branch alone. In order to compare the particle decay

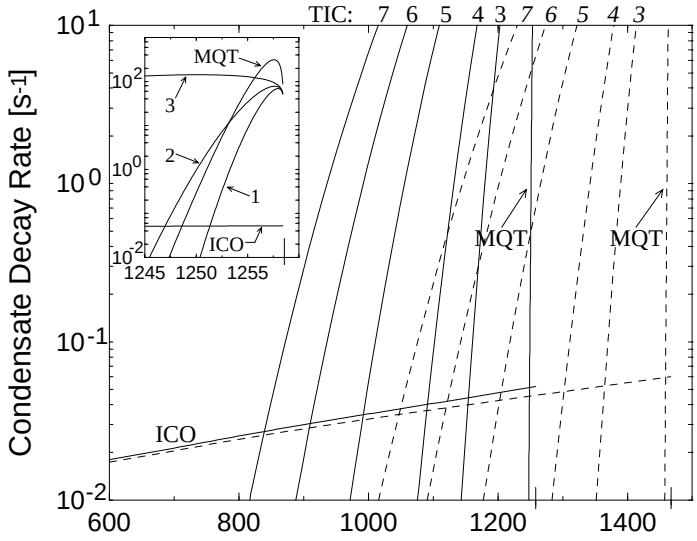

Fig. 24. Condensate decay rates versus particle number. ICO: inelastic collisions. MQT: macroscopic quantum tunneling TIC: thermally induced collapse at temperatures $1nK$ (1),$2nK$(2), $50nK$ (3), $100nK$ (4), $200nK$ (5), $300nK$ (6) and $400nK$ (7). The insert shows the details of the cross-over region between quantum tunneling and thermal decay rate. Solid lines: exact solution of the NLSE equation, dashed lines: Gaussian approximation.

rate $f_C(\mathcal{N})$ to the condensate collective decay rates obtained for TIC and MQT, we compute the condensate ICO half-life as:

$$\tau_{1/2}(\mathcal{N}) = \int_{\mathcal{N}/2}^{\mathcal{N}} dn/f_C(n) \tag{87}$$

and plot $\tau_{1/2}^{-1}$ on Fig. 24.

Discussion

It is apparent by inspection of Fig. 24 that for a given value of $\mathcal{N}$ the exact and Gaussian approximate rates are dramatically different. We now compare the relative importance of the different exact decay rates. At $T \leq 1\,\mathrm{nK}$, the MQT effect becomes important compared to the ICO decay in a region very close to $\mathcal{N}_c^E$ ($\delta \leq 8 \times 10^{-3}$) as was shown in [69] using Gaussian computations but evaluating them with the exact maximal number of condensed particles $\mathcal{N}_c^E$. Considering thermal fluctuations for temperatures as low as $2\,\mathrm{nK}$, it is apparent on Fig. 24 (see insert) that the MQT will be the dominant decay mechanism only in a region extremely close to $\mathcal{N}_c$ ($\delta < 5 \times 10^{-3}$) where the condensates will live less than $10^{-1}\,\mathrm{s}$. Thus, in the experimental case of ^{7}Li atoms, the relevant effects are ICO and TIC, with cross-over determined in Fig. 24.

Calculations similar to those described here have also been generalized to an attractive Bose-Einstein condensate confined by a cylindrically symmetric potential $V(r) = m(\omega_r^2 r^2 + \omega_z^2 z^2)/2$, which lead to cigar-shaped or pancake-shaped condensates. Newton's method was used to calculated stationary states, as described above. The inverse Arnoldi method was used to calculate the leading eigenvalues $\lambda_\pm^2$, yielding decay rates that are similar to those computed for the spherically symmetric case. This was found to be due to spontaneous isotropization of the condensates. See [18] for more details.

5 Conclusion

The main result of the NLSE simulations presented in section 3.2 is that two diagnostics of Kolmogorov's regime in decaying turbulence are satisfied. These diagnostics are, at the time of the maximum of energy dissipation: (i) a parameter-independent kinetic energy dissipation rate and (ii) a $k^{-5/3}$ spectral scaling in the inertial range. Thus, the NLSE simulations were shown to be very similar, as far as energetics is concerned, with the viscous simulations. The experimental results presented in section 3.3 prove that the Kolmogorov cascade survives in the superfluid regime.

We have seen that the numerical tools developed in section 4.3 can be used in practice to obtain the stationary solutions of the NLSE. These methods have allowed us to find the full bifurcation diagrams of Bose-Einstein condensates with attractive interactions and superflows past a cylinder. Furthermore, the stationary solutions have given us efficient way to start vortical dynamics (in 2D and 3D) in a controlled manner.

6 Acknowledgments

The work reviewed in this paper was performed in collaboration with G. Dewel, J. Maurer and P. Tabeling. It was supported by ECOS-CONICYT program no. C01E08 and by the NSF DMR 0094569. Computations were performed at the Institut du Développement et des Ressources en Informatique Scientifique.

References

[1] R. J. Donnelly. *Quantized Vortices in Helium II.* Cambridge Univ. Press, Cambridge, 1991.

[2] E.P. Gross. Structure of a quantized vortex in boson systems. *Nuovo Cimento*, 20(3), 1961.

[3] L.P. Pitaevskii. Vortex lines in an imperfect Bose gas. *Sov. Phys.-JETP*, 13(2), 1961.

[4] L. Landau and E. Lifchitz. *Fluid Mechanics*. Pergamon Press, Oxford, 1980.

[5] M. H. Anderson, J. R. Ensher, M. R. Matthews, C. E. Wieman, and E. A. Cornell. Observation of Bose-Einstein condensation in a dilute atomic vapor. *Science*, 269:198, 1995.

[6] K. B. Davis, M. O. Mewes, M. R. Adrews, N. J. van Druten, D. S. Durfee, D. M. Kurn, and W. Ketterle. Bose-Einstein condensation in a gas of sodium atoms. *Phys. Rev. Lett.*, 75:3969, 1995.

[7] C. C. Bradley, C. A. Sackett, and R. G. Hulet. Bose-Einstein condensation of lithium: Observation of limited condensate number. *Phys. Rev. Lett.*, 78(6):985, 1997.

[8] F. Dalfovo, S. Giorgini, L. P. Pitaevskii, and S. Stringari. Theory of Bose-Einstein condensation in trapped gases. *Rev. Mod. Physics*, 71(3), 1999.

[9] Y. Pomeau and S. Rica. Model of superflow with rotons. *Phys. Rev. Lett.*, 71,2:247, 1993.

[10] P.H. Roberts and N.G. Berloff. The nonlinear Schrödinger equation as a model of superfluidity. In C. F. Barenghi, R. J. Donnelly, and W. F. Vinen, editors, *Quantized vortex dynamics and superfluid turbulence*, pages 235–256. Lecture Notes in Physics, 2001.

[11] C. Nore, M. Abid, and M. Brachet. Decaying kolmogorov turbulence in a model of superflow. *Phys. Fluids*, 9(9):2644, 1997.

[12] C. Nore, M. Abid, and M. E. Brachet. Kolmogorov turbulence in low-temperature superflows. *Phys. Rev. Lett.*, 78(20):3896–3899, 1997.

[13] M. Abid, M. Brachet, J. Maurer, C. Nore, and P. Tabeling. Experimental and numerical investigations of low–temperature superfluid turbulence. *Eur. J. Mech. B Fluids*, 17(4):665–675, 1998.

[14] C. Huepe and M.-E. Brachet. Solutions de nucléation tourbillonnaires dans un modèle d'écoulement superfluide. *C. R. Acad. Sci. Paris*, 325(II):195–202, 1997.

[15] C. Huepe and M. E. Brachet. Scaling laws for vortical nucleation solutions in a model of superflow. *Physica D*, 140:126–140, 2000.

[16] C. Nore, C. Huepe, and M. E. Brachet. Subcritical dissipation in three-dimensional superflows. *Phys. Rev. Lett.*, 84(10):2191, 2000.

[17] C. Huepe, S. Métens, G. Dewel, P. Borckmans, and M.-E. Brachet. Decay rates in attractive Bose-Einstein condensates. *Phys. Rev. Lett.*, 82(2):1616, 1999.

[18] C. Huepe, L.S. Tuckerman, S. Métens, and M.-E. Brachet. Stability and decay rates of non-isotropic attractive Bose-Einstein condensates. *Phys. Rev. A*, in press.

[19] W.F. Vinen and J.J. Niemela. Quantum turbulence. *Jour. Low Temp. Phys.*, 128:167–231, 2002.

[20] C. F. Barenghi, R. J. Donnelly, and W. F. Vinen, editors. *Quantized vortex dynamics and superfluid turbulence*. Lecture Notes in Physics, 2001.

[21] T. Araki, M. Tsubota, and S. K. Nemirovskii. Energy spectrum of superfluid turbulence with no normal-fluid component. *Phys. Rev. Lett.*, 89,14:1–4, 2002.

[22] S.I. Ogawa, M. Tsubota, and Y. Hattori. Study of reconnection and acoustic emission of quantized vortices in superfluid by the numerical analysis of the Gross-Pitaevskii equation. *J. Phys. Soc. Jpn*, 71:813, 2002.

[23] J. Koplik and H. Levine. Vortex reconnection in superfluid Helium. *Phys. Rev. Lett.*, 71:1375–1378, 1993.

[24] T. Araki and M. Tsubota. Cascade process of vortex tangle dynamics in superfluid ^{4}He without mutual friction. *J. Low Temp. Phys.*, 121:405, 2000.

[25] M. Leadbeater, D.C. Samuels, C.F. Barenghi, and C.S. Adams. Decay of superfluid turbulence via Kelvin-wave radiation. *Phys. Rev. A*, 67:015601–1, 2003.

[26] D. Kivotides, J.C.Vassilicos, D.C. Samuels, and C.F. Barenghi. Kelvin waves cascade in superfluid turbulence. *Phys. Rev. Lett.*, 86:3080–3083, 2001.

[27] B. V. Svistunov. Superfluid turbulence in the low-temperature limit. *Phys. Rev. B*, 52:3647, 1995.

[28] W.F. Vinen. Decay of turbulence at a very low temperature: the radiation of sound from a Kelvin wave on a quantized vortex. *Phys. Rev. B*, 64:134520–1, 2001.

[29] S.I. Davis, P.C. Hendry, and P.V.E. McClintock. Decay of quantized vorticity in superfluid ^{4}He at mK temperature. *Physica B*, 280:43–44, 2000.

[30] M. R. Matthews, B. P. Anderson, P. C. Haljan, D. S. Hall, C. E. Wieman, and E. A. Cornell. Vortices in a Bose-Einstein condensate. *Phys. Rev. Lett.*, 83:2498–2501, 1999.

[31] S. Inouye, S. Gupta, T. Rosenband, A.P. Chikkatur, A. Görlitz, T.L. Gustavson, A.E. Leanhardt, D.E. Pritchard, and W. Ketterle. Observation of vortex phase singularities in Bose-Einstein condensates. *Phys. Rev. Lett.*, 87:080402, 2001.

[32] K. W. Madison, F. Chevy, W. Wohlleben, and J. Dalibard. Vortex formation in a stirred Bose-Einstein condensate. *Phys. Rev. Lett.*, 84:806–809, 2000.

[33] P. Rosenbush, V. Bretin, and J. Dalibard. Dynamics of a single vortex line in a Bose-Einstein condensate. *Phys. Rev. Lett.*, 89:200403–1, 2002.

[34] V. Bretin, P. Rosenbush, F. Chevy, G.V. Shlyapnikov, and J. Dalibard. Quadrupole oscillation of a single-vortex condensate: evidence for Kelvin modes. *condmat*, page 0211101, 2003.

[35] E. A. Spiegel. Fluid dynamical form of the linear and nonlinear Schrödinger equations. *Physica D*, 1:236, 1980.

[36] P. Nozières and D. Pines. *The Theory of Quantum Liquids.* Addison Wesley, New York, 1990.

[37] C. Nore, M. Brachet, and S. Fauve. Numerical study of hydrodynamics using the nonlinear Schrödinger equation. *Physica D*, 65:154–162, 1993.

[38] D. Gottlieb and S. A. Orszag. *Numerical Analysis of Spectral Methods.* SIAM, Philadelphia, 1977.

[39] M. P. Kawatra and R. K. Pathria. Quantized vortices in imperfect Bose gas. *Phys.Rev.*, 151:1, 1966.

[40] K. W. Schwarz. Three-dimensional vortex dynamics in superfluid ^{4}He: line-line and line-boundary interactions. *Phys. Rev. B*, 31:5782, 1985.

[41] J. C. Neu. Vortices in complex scalar fields. *Physica D*, 43:385, 1990.

[42] F. Lund. Defect dynamics for the nonlinear Schrödinger equation derived from a variational principle. *Phys.Rev.Lett.*, A 159:245, 1991.

[43] G. I. Taylor and A. E. Green. Mechanism of the production of small eddies from large ones. *Proc. Soc. Lond. A*, 158:499, 1937.

[44] M. E. Brachet, D. I. Meiron, S. A. Orszag, B. G. Nickel, R. H. Morf, and U. Frisch. Small-scale structure of the Taylor-Green vortex. *J. Fluid Mech.*, 130:411–452, 1983.

[45] M. Brachet. Géométrie des structures à petite échelle dans le vortex de Taylor-Green. *C.R.A.S II*, **311**:775, 1990.

[46] J. Domaradzki, W. Liu, and M. Brachet. An analysis of sugrid-scale interactions in numerically simulated isotropic turbulence. *Phys. Fluids A*, 5:1747, 1993.

[47] C. Nore, M. Abid, and M. Brachet. Simulation numérique d'écoulements cisaillés tridimensionnels à l'aide de l'équation de Schrödinger non linéaire. *C.R.A.S*, 319 II(7):733, 1994.

[48] U. Frisch. *Turbulence, the legacy of A. N. Kolmogorov.* Cambridge Univ. Press, Cambridge, 1995.

[49] T. Araki, M. Tsubota, and S. K. Nemirovskii. Energy spectrum of superfluid turbulence with no normal-fluid component. *Phys. Rev. Lett.*, 89,14:1–4, 2002.

[50] S. Douady, Y. Couder, and M. E. Brachet. Direct observation of the intermittency of intense vorticity filaments in turbulence. *Phys. Rev. Lett.*, 67:983, 1991.

[51] G. Zocchi, P. Tabeling, J. Maurer, and H. Willaime. Measurement of the scaling of the dissipation at high Reynolds numbers. *Phys. Rev. E*, 50:3693, 1994.

[52] S. Fauve, C. Laroche, and B. Castaing. Pressure fluctuations in swirling turbulent flows. *J. Phys. II*, 3:271, 1993.

[53] J. Maurer and P. Tabeling. Local investigation of superfluid turbulence. *Europhys. Lett.*, 43(1):29–34, 1998.

[54] V. Hakim. Nonlinear Schrödinger flow past an obstacle in one dimension. *Phys. Rev. E*, 55(3):2835–2845, 1997.

[55] T. Tsuzuki. Nonlinear waves in the Pitaevskii-Gross equation. *J. Low Temp. Phys.*, 4(4), 1971.

[56] V.E. Zakharov and A.B. Shabat. Interaction between solitons in a stable medium. *Sov. Phys.-JETP*, 37(5):823–828, 1973.

[57] C.-T. Pham and M. Brachet. Dynamical scaling laws in two types of extended hamiltonian systems at dissipation onset. *Physica D*, 163:129–147, 2002.

[58] R. Seydel. *From Equilibrium to Chaos: Practical Bifurcation and Stability Analysis*. Elsevier, New York, 1988.

[59] C. Mamun and L. Tuckerman. Asymmetry and Hopf bifurcation in spherical Couette flow. *Phys. Fluids*, 7(1):80, 1995.

[60] W. Press, S. Teukolsky, W. Vetterling, and B.Flannery. *Numerical Recipees in Fortran*. Cambridge Univ. Press, Cambridge, 1994.

[61] H. van der Vorst. Bi-cgstab: A fast and smoothly converging variant of bi-cg for the solution of nonsymmetric linear systems. *SIAM J. Sci. Stat. Comput.*, 13:631, 1992.

[62] R. Klein and A. J. Majda. Self-stretching of perturbed vortex filaments. *Physica D*, 53:267, 1991.

[63] T. Frisch, Y. Pomeau, and S. Rica. Transition to dissipation in a model of superflow. *Phys.Rev.Lett.*, 69:1644, 1992.

[64] O. Avenel, G.G. Ihas, and E. Varoquaux. The nucleation of vortices in superfluid ^{4}He: Answers and questions. *J. Low Temp.Phys.*, 93:1031–1057, 1993.

[65] G.G. Ihas, O. Avenel, R. Aarts, R Salmelin, and E. Varoquaux. Quantum nucleation of vortices in the flow of superfluid He-4 through an orifice. *Phys. Rev. Lett.*, 69(2):327, 1992.

[66] C. A. Jones and P. H. Roberts. Motions in a bose condensate: Iv. axisymmetric solitary waves. *J. Phys. A*, 15:2599, 1982.

[67] J. Wilks. *The properties of liquid and solid helium*. Clarendon Press, Oxford, 1967.

[68] C. Raman, M. Köhl, R. Onofrio, D.S. Durfee, C.E. Kuklewicz, Z. Hadzibabic, and W. Ketterle. Evidence for a critical velocity in a Bose-Einstein condensed gas. *Phys. Rev. Lett.*, 83(13):2502, 1999.

[69] M. Ueda and A. J. Leggett. Macroscopic quantum tunneling of a Bose-Einstein condensate with attractive interaction. *Phys. Rev. Lett.*, 80(8):1576, 1998.

[70] H. T. C. Stoof. Macroscopic quantum tunneling of a Bose condensate. *J. Stat. Phys.*, 87:1353, 1997.

[71] H. Shi and W.-M. Zheng. Bose-Einstein condensation in an atomic gas with attractive interactions. *Phys. Rev. A*, 55(4):2930, 1997.

[72] R. J. Dodd, M. Edwards, C. J. Williams, C. W. Clark, M. J. Holland, P. A. Ruprecht, and K. Burnett. Role of attractive interactions on Bose-Einstein condensation. *Phys. Rev. A*, 54(1):661, 1996.

[73] C. A. Sackett, H. T. C. Stoof, and R. G. Hulet. Growth and collapse of a Bose-Einstein condensate with attractive interactions. *Phys. Rev. Lett.*, 80(10):2031, 1998.

[74] C. Huepe. *Bifurcations et instabilités dans les condensats de Bose-Einstein et les écoulements superfluides*. PhD thesis, Ecole Normale Supérieure, 1999.

[75] J. Guckenheimer and P. Holmes. *Nonlinear Oscillations, Dynamical Systems and Bifurcations of Vector Fields*. Springer-Verlag, Berlin, 1983.

[76] C. C. Bradley, C. A. Sackett, J. J. Tollett, and R. G. Hulet. Evidence of Bose-Einstein condensation in an atomic gas with attractive interactions. *Phys. Rev. Lett.*, 75(9):1687, 1995.

[77] P. A. Ruprecht, M. J. Holland, K. Burnett, and M. Edwards. Time-dependent solution of the nonlinear Schrödinger equation for Bose-condensed trapped neutral atoms. *Phys. Rev. A*, 51(6):4704, 1995.

[78] C.W. Gardiner. *Handbook of Stochastic Methods*. Springer-Verlag, Berlin, 1985.